*J. Fluid Mech.* (2018), *vol.* 835, *pp.* 170–216.  
doi:10.1017/jfm.2017.750

# Effect of temperature gradient on the cross-stream migration of a surfactant-laden droplet in Poiseuille flow

**Sayan Das[1], Shubhadeep Mandal[1] and Suman Chakraborty[1,†]**

[1]Department of Mechanical Engineering, Indian Institute of Technology, Kharagpur, Kharagpur – 721302, India

(Received 18 April 2017; revised 24 August 2017; accepted 10 October 2017; first published online 27 November 2017)

The motion of a viscous droplet in unbounded Poiseuille flow under the combined influence of bulk-insoluble surfactant and linearly varying temperature field aligned in the direction of imposed flow is studied analytically. Neglecting fluid inertia, thermal convection and shape deformation, asymptotic analysis is performed to obtain the velocity of a force-free surfactant-laden droplet. The droplet speed and direction of motion are strongly influenced by the interfacial transport of surfactant, which is governed by surface Péclet number. The present study is focused on the following two limiting situations of surfactant transport: (i) surface-diffusion-dominated surfactant transport considering small surface Péclet number, and (ii) surface-convection-dominated surfactant transport considering high surface Péclet number. Thermocapillary-induced Marangoni stress, the strength of which relative to viscous stress is represented by the thermal Marangoni number, has a strong influence on the distribution of surfactant on the droplet surface. The present study shows that the motion of a surfactant-laden droplet in the combined presence of temperature and imposed Poiseuille flow cannot be obtained by a simple superposition of the following two independent results: migration of a surfactant-free droplet in a temperature gradient, and the motion of a surfactant-laden droplet in a Poiseuille flow. The temperature field not only affects the axial velocity of the droplet, but also has a non-trivial effect on the cross-stream velocity of the droplet in spite of the fact that the temperature gradient is aligned with the Poiseuille flow direction. When the imposed temperature increases in the direction of the Poiseuille flow, the droplet migrates towards the flow centreline. The magnitude of both axial and cross-stream velocity components increases with the thermal Marangoni number. However, when the imposed temperature decreases in the direction of the Poiseuille flow, the magnitude of both axial and cross-stream velocity components may increase or decrease with the thermal Marangoni number. Most interestingly, the droplet moves either towards the flow centreline or away from it. The present study shows a critical value of the thermal Marangoni number beyond which the droplet moves away from the flow centreline which is in sharp contrast to the motion of a surfactant-laden droplet in isothermal flow, for which the droplet always moves towards the flow centreline. Interestingly, we show that the above picture may become significantly altered in the case where the droplet is not a neutrally buoyant one. When the droplet is less dense than the suspending medium, the presence of gravity in the

†Email address for correspondence: suman@mech.iitkgp.ernet.in

direction of the Poiseuille flow can lead to cross-stream motion of the droplet away from the flow centreline even when the temperature increases in the direction of the Poiseuille flow. These results may bear far-reaching consequences in various emulsification techniques in microfluidic devices, as well as in biomolecule synthesis, vesicle dynamics, single-cell analysis and nanoparticle synthesis.

**Key words:** drops, thermocapillarity

## 1. Introduction

The dynamics of suspending droplets has been a recent topic of interest to the science and engineering community, due to its wide gamut of applications in microfluidic devices (Stone, Stroock & Ajdari 2004; Baroud, Gallaire & Dangla 2010; Seemann *et al.* 2012). In such devices, droplets are used in analytic detection, reagent mixing, drug delivery and cell encapsulation process, to name a few (Di Carlo *et al.* 2007; Huebner *et al.* 2008; Teh *et al.* 2008; Baroud *et al.* 2010; Zhu & Fang 2013). It also has wide applications in biomolecule synthesis, vesicle dynamics, single-cell analysis and nanoparticle synthesis (Huebner *et al.* 2008; Teh *et al.* 2008; Casadevall i Solvas & deMello 2011; Seemann *et al.* 2012; Shields, Reyes & López 2015). In addition, one may mention other relevant industrial processes such as pumping of slurries (Karabelas 1977; Kaushal & Tomita 2002) and biological processes such as the lateral migration and positioning of erythrocytes in the blood circulatory system (Fåhraeus 1929; Pries, Secomb & Gaehtgens 1996). In fact, proper control as well as understanding of the position of the dispersed phase (or particles) in a laminar fluid flow opens up a wide variety of scopes in terms of flow cytometry (Bonner *et al.* 1972) or flow field fractionation (Giddings 1993; Yang *et al.* 1999).

In a wide gamut of microfluidic devices, suspended droplets are transported along the flow with the aid of syringe pumps (Stan *et al.* 2011). The control over droplet migration in such devices can be acquired from the knowledge of flow geometry and fluid properties. However, this control over the lateral migration can be fine-tuned by the application of an external temperature gradient in the flow field. This non-uniform temperature distribution in the flow field can be utilized in microfluidic devices for the purpose of sorting and separation of droplets (Baroud *et al.* 2007; Robert de Saint Vincent, Wunenburger & Delville 2008; Miralles *et al.* 2013).

Surfactants (or surface-active agents) are common in different droplet-based devices. Surfactants are used as additives in droplet-based systems to enhance droplet generation and the stability of emulsions (Baret 2012). The presence of surfactants at the droplet interface not only lowers the interfacial tension but also can induce a Marangoni stress if the spatial variation of surfactants is non-uniform (Leal 2007). So, to perform optimal functionalities of the concerned devices, a fundamental understanding of the motion of surfactant-laden droplet is of prime importance.

Several theoretical and experimental works have been performed to study the motion of droplets in Poiseuille flow (Leal 1980; Stan *et al.* 2011; Chen *et al.* 2014). In the creeping-flow limit, a non-deformable, spherical, Newtonian droplet suspended in another Newtonian fluid with a clean fluid–fluid interface moves in the direction of flow in an unbounded Poiseuille flow (Hetsroni & Haber 1970). This can be well explained by the symmetry-under-flow-reversal argument, which is valid for linear governing equations and boundary conditions (Leal 2007). Interesting things happen

in the presence of nonlinear effects such as deformation, viscoelasticity and inertia. A deformable droplet not only moves in the direction of flow, but also moves in the cross-stream direction (Haber & Hetsroni 1971; Wohl & Rubinow 1974; Chan & Leal 1979; Mortazavi & Tryggvason 2000; Griggs, Zinchenko & Davis 2007; Mandal, Bandopadhyay & Chakraborty 2015). Chan & Leal (1979) have found that a deformable droplet moves towards the channel centreline when $\lambda < 0.5$ or $\lambda > 10$ (where $\lambda$ is the droplet to medium viscosity ratio), while droplet moves away from the centreline when $0.5 < \lambda < 10$. Several studies have also reported cross-stream migration of non-deformable droplets in Poiseuille flow in the presence of fluid inertia (Karnis, Goldsmith & Mason 1966; Hur *et al.* 2011; Chen *et al.* 2014) or fluid viscoelasticity (Chan & Leal 1979; Mukherjee & Sarkar 2013, 2014). These deformation-, inertia- and viscoelasticity-induced cross-stream migration characteristics are used in microfluidic devices as sorting mechanisms (Hatch *et al.* 2013; Amini, Lee & Di Carlo 2014; Sajeesh & Sen 2014). Very recently, Hanna & Vlahovska (2010) and Pak, Feng & Stone (2014) have found that surfactant-induced Marangoni stress at the droplet interface can induce a cross-stream migration of a spherical droplet in Poiseuille flow even in the absence of deformation, inertia and viscoelasticity.

Studies on droplet motion in the presence of external effects such as electric (Ahn *et al.* 2006; Link *et al.* 2006; Bandopadhyay *et al.* 2016; Mandal, Bandopadhyay & Chakraborty 2016), magnetic (Seemann *et al.* 2012), temperature (Karbalaei, Kumar & Cho 2016) and acoustic fields (Seemann *et al.* 2012) are gaining much importance nowadays due to the ease with which these fields can be applied in respective applications. The presence of these fields induces an imbalance in stresses at the droplet interface and modifies the net force acting on the droplet, which in turn alters the droplet velocity and associated flow field. Out of all the effects mentioned above, in the present study we focus on the effect of a temperature field. The variation of the temperature field across the droplet induces Marangoni stress at the droplet interface, which induces droplet motion even in the absence of an imposed flow (Young, Goldstein & Block 1959). Following Young *et al.* (1959), several studies have considered the thermocapillary motion of a droplet in a quiescent medium to study the following aspects: droplet deformation (Nadim, Haj-Hariri & Borhan 1990), fluid inertia (Haj-Hariri, Nadim & Borhan 1990), thermal convection (Zhang, Subramanian & Balasubramaniam 2001; Balasubramaniam & Subramanian 2004; Yariv & Shusser 2006) and bounding walls (Meyyappan & Subramanian 1987; Barton & Shankar Subramanian 1990; Barton & Subramanian 1991; Chen 1999, 2003). In recent studies, Raja Sekhar and co-workers have investigated the effect of thermocapillary-induced Marangoni stress on the droplet velocity in the presence of an imposed flow field (Choudhuri & Raja Sekhar 2013; Sharanya & Raja Sekhar 2015). In the absence of shape deformation, surfactants and fluid inertia, their studies show that the effects of a temperature field and an imposed background flow can be linearly combined to obtain the final droplet velocity.

In a recent work, we have investigated the axisymmetric motion of a surfactant-laden droplet in the combined presence of a linearly varying temperature field and an imposed Poiseuille flow (Das *et al.* 2017). However, there is no study present in the literature which investigates the combined effect of temperature and an imposed Poiseuille flow on the cross-stream migration characteristics of a droplet in the presence of bulk-insoluble surfactants. In the present study, we analytically obtain the droplet velocity in an unbounded Poiseuille flow considering both thermocapillary-induced and surfactant-induced Marangoni stresses at the droplet interface. We show that in the presence of a non-uniform surfactant distribution at the

droplet interface, the effects of a temperature field and an imposed background flow cannot be linearly combined to obtain the final droplet velocity. By neglecting fluid inertia, thermal convection and shape deformation, we perform asymptotic analysis for two different limits: (i) when the surface diffusion of the surfactants dominates interfacial transport, and (ii) when the surface convection of the surfactants dominates interfacial transport, in an effort to unveil the mechanisms of cross-stream migration of the droplet.

Interestingly, we have pinpointed that the sole reason for the cross-stream droplet velocity to be dependent on the axial temperature gradient is the coupled nonlinear nature of the governing equations (the surfactant transport equation and Stokes equations). This applied temperature gradient results in a jump in tangential stress across the interface in addition to the jump induced by the non-uniform distribution of surfactants. Although the consequent implications are apparently of second order, the results due to the presence of a temperature gradient or buoyancy are non-intuitive. The present study shows that a temperature gradient can solely influence the axial migration of a surfactant-free droplet, regardless of whether it is placed eccentrically or not. On the contrary, it is further intriguing that when the drop is covered with bulk-insoluble surfactants, the thermocapillary effect is not simply 'additive' but also 'multiplicative', in a sense that it couples with the non-uniform surfactant distributions to non-trivially influence the axial and cross-streamline droplet dynamics. As a result, an applied temperature gradient has a non-trivial contribution towards axial and cross-stream dynamics of a surfactant-covered droplet. To mimic physically relevant situations, we analyse the droplet migration characteristic for both buoyant and neutrally buoyant droplets. It is seen that a denser droplet always migrates towards the flow centreline if a temperature gradient is applied in the direction of the imposed flow. However, considering the special case when the carrier phase has higher density, the droplet may migrate away from the centreline of flow although a temperature gradient is applied in the direction of the imposed flow. For a neutrally buoyant system or a sufficiently low density difference between either phases, the applied temperature gradient becomes the governing factor for the direction of cross-stream migration of the droplet.

## 2. Problem formulation

### 2.1. *System description*

The present system consists of a spherical, Newtonian droplet (density $\rho_i$, viscosity $\mu_i$, and thermal conductivity $k_i$) of radius $a$ suspended in another Newtonian medium (density $\rho_e$, viscosity $\mu_e$, and thermal conductivity $k_e$). Bulk-insoluble surfactants are present at the droplet interface. All the material properties are assumed to be constant, except the interfacial tension ($\bar{\sigma}$). The interfacial tension depends on the interface temperature ($\bar{T}_s$) and the local surfactant concentration ($\bar{\Gamma}$) along the interface of the droplet. In a quiescent medium, the surfactants are uniformly distributed over the droplet surface. The concentration of surfactant at equilibrium is denoted by $\bar{\Gamma}_{eq}$ and the corresponding interfacial tension is denoted by $\bar{\sigma}_{eq}$. This equilibrium is disturbed by application of a background Poiseuille flow ($\bar{\boldsymbol{V}}_\infty$) and a linearly varying temperature field ($\bar{T}_\infty$). The imposed Poiseuille flow alters the interfacial tension via the convection of surfactants at the droplet interface. On the other hand, the effect of the temperature field on the interfacial tension is twofold: (i) it directly alters the interfacial tension, as interfacial tension is a function of temperature at the

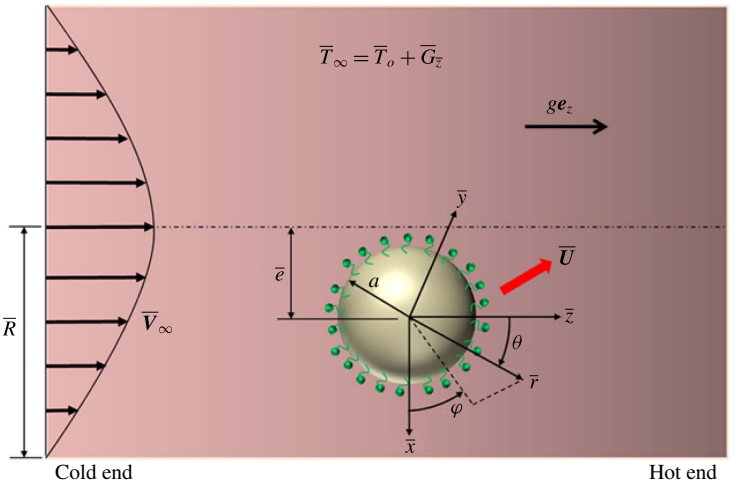


FIGURE 1. (Colour online) Schematic of a surfactant-laden droplet of radius $a$ suspended in a cylindrical Poiseuille flow ($\bar{V}_\infty$). The imposed temperature field ($\bar{T}_\infty$) varies linearly in the axial direction ($\bar{z}$-direction). The droplet is placed at an eccentric location of distance $\bar{e}$ from the channel centreline and is acted upon by a gravitational acceleration $g$. Both spherical $(r, \theta, \varphi)$ and Cartesian $(\bar{x}, \bar{y}, \bar{z})$ coordinates are shown. It is important to note that the $\bar{x}$ axis is always directed outwards from the channel centreline.

droplet interface, and (ii) thermocapillary-induced Marangoni stress induces transport of surfactants at the droplet interface.

In several practical situations, the droplet can have density different from that of the suspending medium. In the presence of gravity, the buoyancy effect leads to motion of the droplet. Gravity can act normal or parallel to the direction of the Poiseuille flow. When the gravity acts in the direction normal to the Poiseuille flow, the cross-stream velocity of a buoyant droplet is strongly governed by the buoyancy force, while the effects of Poiseuille flow and temperature field are negligible. Thus, the study of buoyant droplets in these kinds of system are of less importance. Here we explore droplet migration when gravity is acting in the direction of the imposed Poiseuille flow (refer to figure 1). So, the combined presence of Poiseuille flow, gravity, surface tension and temperature field leads to the generation of Marangoni stresses which will affect the droplet velocity ($\bar{\boldsymbol{U}}$). The main objective of the present study is to investigate the effect of the Marangoni stresses on the droplet velocity. Towards this, we consider a spherical coordinate system $(\bar{r}, \theta, \varphi)$ which is attached at the droplet centroid (refer to figure 1). A Cartesian coordinate system $(\bar{x}, \bar{y}, \bar{z})$ is also shown attached to the droplet. The gravitational force acts in the axial direction ($\bar{z}$-direction).

### 2.2. *Assumptions*

The major assumptions made in this study to simplify the governing equations and the boundary conditions are as follows: (i) the thermal problem is governed by the conduction of heat, which is based on the fact that the thermal Péclet number ($Pe_T = \bar{V}_c a/\alpha_e$, where $\alpha_e$ is the thermal diffusivity of the suspending medium and $\bar{V}_c$ is the centreline velocity of imposed Poiseuille flow) is small enough so that the advective transport of thermal energy is negligible. (ii) The flow problem is governed by the viscous and pressure forces. This is based on the fact that

the Reynolds number ($Re = \rho \bar{V}_c a/\mu_e$) is small enough so that the fluid inertia is negligible. (iii) The droplet shape is considered as a perfect sphere. This is based on the fact that capillary number ($Ca = \mu_e \bar{V}_c/\bar{\sigma}_o$) is small enough so that the interfacial tension dominates over the viscous stresses. (iv) The surfactants are insoluble in the bulk fluid (Baret 2012). (v) The surfactant distribution along the interface of the droplet does not affect the heat transfer process (Kim & Subramanian 1989*b*). (vi) The interfacial tension is linearly dependent on the temperature and the surfactant concentration at the interface of the droplet (Homsy & Meiburg 1984; Carpenter & Homsy 1985). (vii) We consider the imposed Poiseuille flow to be a unbounded one, which disregards the effects of bounding walls. (viii) Any effect of natural convection in the system under consideration is neglected. This can be said based on the fact that the magnitude of both Grashof number ($Gr = g\gamma_e \rho_e^2 \Delta T a^3/\mu_e^2$) and Rayleigh number ($Ra = g\gamma_e \rho_e \Delta T a^3/\mu_e \alpha_e$) are very small ($Gr, Ra \ll 1$) for the present system. Here $\Delta T$ is the characteristic temperature difference, and $\gamma_e$ is the volumetric expansion coefficient of the carrier phase due to an increase in temperature.

### 2.3. *Experimental perspective*

The typical values of the non-dimensional numbers can be obtained from the existing experimental data (Nallani & Subramanian 1993; Chen *et al.* 1997). Nallani & Subramanian (1993) have performed experiments on the thermocapillary motion of a methanol droplet of radius 50 μm suspended in silicone oil (with $\rho_e = 955$ kg m$^{-3}$, $\mu_e = 0.0478$ Ns m$^{-2}$, $\gamma_e = 0.0007\,^{\circ}\mathrm{C}^{-1}$, $k_e = 0.1$ W mK$^{-1}$ and $c_{pe} = 1800$ J kg$^{-1}$ K$^{-1}$) which is an example of a buoyant system. Chen *et al.* (1997), on the other hand, performed experiments on the thermocapillary migration of a surfactant-laden droplet for a neutrally buoyant system. This system is composed of water as the droplet phase and *n*-butyl benzoate (with $\rho_e = 995$ kg m$^{-3}$, $\mu_e = 2.49 \times 10^{-3}$ Ns m$^{-2}$, $\gamma_e = 0.00125\,^{\circ}\mathrm{C}^{-}$, $\alpha_e = 6.63 \times 10^{-8}$ m$^2$ s$^{-1}$) as the carrier phase. All the property values above are measured at a temperature of 32 °C. The density of distilled water at 32 °C is 995.03 kg m$^{-3}$ whereas the density of *n*-butyl benzoate at the same temperature according to Hähnel, Delitzsch & Eckelmann (1989) is 995.02 kg m$^{-3}$. We consider $\bar{V}_c = 10^{-4}$ m s$^{-1}$ (which is common in microfluidic devices), $a = 50$ μm, a characteristic temperature difference of $\Delta T = 2\,^{\circ}\mathrm{C}$ and $\bar{\sigma}_o = 10^{-3}$ N m$^{-1}$ for a methanol–silicone oil system and $\bar{\sigma}_o = 22.76 \times 10^{-3}$ N m$^{-1}$ for a water-*n*-butyl benzoate system. Using the above property values as obtained from the experimental works done by Nallani & Subramanian (1993) and Chen *et al.* (1997) we obtain the following values of the different non-dimensional parameters as given in table 1. It is apparent from table 1 that the consideration of negligible thermal convection (both buoyancy driven and imposed flow driven), fluid inertia and shape deformation is justified. The typical values of other non-dimensional parameters are mentioned as they appear.

The Bond number (*Bo*) is the ratio of the gravitational force to the surface tension force acting on the droplet in the flow field and is discussed in detail later. The present problem can investigated from an experimental perspective as well. However, there is no experimental study present in the literature that takes into account the temperature-induced cross-stream migration of a surfactant-laden droplet. Towards this, we provide a brief outline of a possible experimental design for this purpose. A mechanism for droplet generation in a microfluidic channel has to be developed whose job will be to release the droplet in a larger channel at an eccentric position with respect to the centreline of the flow. The dispersed phase would consist of water–surfactant solution.

| Non-dimensional numbers | Neutrally buoyant system (droplet phase, water; carrier phase, *n*-butyl benzoate) | Buoyant system (droplet phase, methanol; carrier phase, silicone oil) |
|---|---|---|
| Reynolds number ($Re$) | 0.002 | $9.89 \times 10^{-4}$ |
| Thermal Péclet number ($Pe_T$) | $7.54 \times 10^{-2}$ | $8.6 \times 10^{-2}$ |
| Capillary number ($Ca$) | $0.109 \times 10^{-4}$ | 0.00478 |
| Grashof number ($Gr$) | $4.8952 \times 10^{-4}$ | $6.8526 \times 10^{-6}$ |
| Rayleigh number ($Ra$) | 0.0185 | $5.896 \times 10^{-4}$ |
| Bond Number ($Bo$) | $1.07 \times 10^{-8}$ | 0.004 |

TABLE 1. Values of non-dimensional governing parameters for both buoyant and neutrally buoyant system.

Triton X-100 could be chosen as an appropriate candidate for surfactants. The exit of the channel would consist of a sink at a steady temperature of $T_1$, whereas at the entry another sink will present at a steady temperature $T_2$ such that $T_1 > T_2$. The prime objective of this study will be to measure the cross-stream migration in a certain span of time for different values of $T_1$ with the help of a high-speed camera. The temperature can be varied with the help of a heater that is used to keep the sink at the exit warm. Together with this study, we can also include the effect of buoyancy by considering a buoyant system instead of a neutrally buoyant system. By using silicone oil of different varieties (hence different densities), the buoyancy force on the droplet can be varied as well.

### 2.4. *Governing equations and boundary conditions*

As the thermal Péclet number is small, the thermal problem is governed by a Laplace equation of the form

$$\left.\begin{aligned} \bar{\nabla}^2 \bar{T}_i = 0, \\ \bar{\nabla}^2 \bar{T}_e = 0, \end{aligned}\right\} \tag{2.1}$$

where $\bar{T}_i$ and $\bar{T}_e$ represent the temperature field inside and outside the droplet. Subscripts '$i$' and '$e$' are used to represent quantities inside and outside the droplet, respectively. The temperature field outside the droplet ($\bar{T}_e$) satisfies the far-field condition

$$\text{as } \bar{r} \to \infty, \quad \bar{T}_e = \bar{T}_\infty, \tag{2.2}$$

where $\bar{T}_\infty$ with respect to a spherical coordinate system (origin at the droplet centroid) is represented as

$$\bar{T}_\infty = \bar{T}_o + \bar{G}\bar{z}, \tag{2.3}$$

where $\bar{G}$ is the temperature gradient along $\bar{z}$ and $\bar{T}_o$ is the reference temperature. In the present study, we consider variation of $\bar{T}_\infty$ along the direction of the imposed Poiseuille flow. The imposed temperature increases (or decreases) in the direction of the imposed Poiseuille flow for $\bar{G} > 0$ (or $\bar{G} < 0$). The temperature field inside the droplet ($\bar{T}_i$) is bounded at the centre of the droplet ($\bar{r} = 0$). In addition to these, $\bar{T}_i$ and $\bar{T}_e$ satisfy temperature continuity and heat flux continuity at the droplet surface ($\bar{r} = a$):

$$\left.\begin{aligned} \text{at } \bar{r} = a, \quad \bar{T}_i = \bar{T}_e, \\ \text{at } \bar{r} = a, \quad k_i \frac{\partial \bar{T}_i}{\partial \bar{r}} = k_e \frac{\partial \bar{T}_e}{\partial \bar{r}}. \end{aligned}\right\} \tag{2.4}$$

As the Reynolds number is small, the flow problem is governed by the Stokes and continuity equations in the following form:

$$\left.\begin{aligned} -\bar{\boldsymbol{\nabla}}\bar{p}_i + \mu_i \bar{\nabla}^2 \bar{\boldsymbol{u}}_i = \boldsymbol{0}, \quad \bar{\boldsymbol{\nabla}} \cdot \bar{\boldsymbol{u}}_i = 0, \\ -\bar{\boldsymbol{\nabla}}\bar{p}_e + \mu_e \bar{\nabla}^2 \bar{\boldsymbol{u}}_e = \boldsymbol{0}, \quad \bar{\boldsymbol{\nabla}} \cdot \bar{\boldsymbol{u}}_e = 0, \end{aligned}\right\} \tag{2.5}$$

where $\bar{\boldsymbol{u}}$ and $\bar{p}$ represent the velocity and pressure fields. The velocity and pressure fields outside the droplet satisfy the far-field condition

$$\left.\begin{aligned} \text{as } \bar{r} \to \infty, \quad \bar{\boldsymbol{u}}_e = \bar{\boldsymbol{V}}_\infty - \bar{\boldsymbol{U}}, \\ \text{as } \bar{r} \to \infty, \quad \bar{p}_e = \bar{p}_\infty, \end{aligned}\right\} \tag{2.6}$$

where $\bar{p}_\infty$ is the pressure field associated with $\bar{\boldsymbol{V}}_\infty$. The imposed Poiseuille flow ($\bar{\boldsymbol{V}}_\infty$) with respect to a spherical coordinate system (origin at the droplet centroid) is represented as

$$\bar{\boldsymbol{V}}_\infty = \bar{V}_c \left[1 - \frac{\bar{e}^2}{\bar{R}^2} - \frac{\bar{r}^2}{\bar{R}^2}\sin^2\theta - \frac{2\bar{r}}{\bar{R}^2}\bar{e}\cos\varphi\sin\theta\right]\boldsymbol{e}_z, \tag{2.7}$$

where $\bar{e}$ and $\bar{R}$ are the position of the droplet centroid and the location of zero imposed velocity, which are measured from the centreline of the flow. The velocity and pressure fields inside the droplet ($\bar{\boldsymbol{u}}_i, \bar{p}_i$) are bounded at the centre of the droplet ($\bar{r} = 0$). In addition to these, the velocity and pressure fields satisfy the following interfacial conditions at the droplet surface ($\bar{r} = a$):

$$\left.\begin{aligned} \text{at } \bar{r} = a, \quad \bar{\boldsymbol{u}}_i = \bar{\boldsymbol{u}}_e, \\ \text{at } \bar{r} = a, \quad \bar{\boldsymbol{u}}_i \cdot \boldsymbol{e}_r = \bar{\boldsymbol{u}}_e \cdot \boldsymbol{e}_r = 0, \\ \text{at } \bar{r} = a, \quad (\bar{\boldsymbol{\tau}}_e \cdot \boldsymbol{e}_r - \bar{\boldsymbol{\tau}}_i \cdot \boldsymbol{e}_r) \cdot (\boldsymbol{I} - \boldsymbol{e}_r\boldsymbol{e}_r) = -\bar{\boldsymbol{\nabla}}_s\bar{\sigma}, \end{aligned}\right\} \tag{2.8}$$

where $\bar{\boldsymbol{\tau}}_i = -\bar{p}_i\boldsymbol{I} + \mu_i[\bar{\boldsymbol{\nabla}}\bar{\boldsymbol{u}}_i + (\bar{\boldsymbol{\nabla}}\bar{\boldsymbol{u}}_i)^{\mathrm{T}}]$ and $\bar{\boldsymbol{\tau}}_e = -\bar{p}_e\boldsymbol{I} + \mu_e[\bar{\boldsymbol{\nabla}}\bar{\boldsymbol{u}}_e + (\bar{\boldsymbol{\nabla}}\bar{\boldsymbol{u}}_e)^{\mathrm{T}}]$ represent the hydrodynamic stress tensors inside and outside the droplet, and $\bar{\boldsymbol{\nabla}}_s = [\bar{\boldsymbol{\nabla}} - \boldsymbol{e}_r(\boldsymbol{e}_r \cdot \bar{\boldsymbol{\nabla}})]$ represents the surface gradient operator. The first condition represents the continuity of velocity field, the second condition represents the kinematic condition, and the third condition represents the balance between the tangential component of the hydrodynamic and Marangoni stresses. The normal stress balance is not relevant to the present study as we are considering a spherical droplet shape (Choudhuri & Raja Sekhar 2013).

The Marangoni stress depends on the variation of interfacial tension ($\bar{\sigma}$). Assuming a linear relationship, the dependence of interfacial tension on the temperature and surfactant concentration can be represented as (Homsy & Meiburg 1984; Carpenter & Homsy 1985; Kim & Subramanian 1989*b*)

$$\bar{\sigma} = \bar{\sigma}_o - \beta(\bar{T}_s - \bar{T}_o) - R_g\bar{T}_o\bar{\Gamma}, \tag{2.9}$$

where $\bar{\sigma}_o$ is the interfacial tension at the reference temperature $\bar{T}_o$ in the absence of any surfactant, $\bar{T}_s = \bar{T}_i|_{\bar{r}=a}$ is the temperature at the droplet surface, $R_g$ is the ideal gas constant, and $\beta = -\mathrm{d}\bar{\sigma}/\mathrm{d}\bar{T}_s$. The linear dependence of interfacial tension on the local surfactant concentration can be derived from the general relationship between $\bar{\sigma}$ and

$\bar{\Gamma}$, which is obtained from the Langmuir and the Gibbs adsorption isotherm and is given by (Leal 2007)

$$\bar{\sigma} = \bar{\sigma}_o + R_g \bar{T}_o \bar{\Gamma}_{eq} \left[ \ln \left( 1 - \frac{\bar{\Gamma}}{\bar{\Gamma}_{eq}} \right) \right]. \tag{2.10}$$

The above nonlinear relationship between the interfacial tension and surfactant concentration in the limiting case of low or dilute surfactant concentration ($\lim \bar{\sigma}_{\bar{\Gamma} \to 0}$) is given by the linear relationship: $\bar{\sigma} = \bar{\sigma}_o - R_g \bar{T}_o \bar{\Gamma}$. Note that such a simplification is commonly performed to simplify the mathematical calculations. Similar simplifications can be found in several reported studies (Stone & Leal 1990; Vlahovska, Bławzdziewicz & Loewenberg 2009; Pak *et al.* 2014). The surfactant concentration ($\bar{\Gamma}$) at the droplet surface is governed by the following convection–diffusion equation (Stone 1990; Stone & Leal 1990):

$$\bar{\nabla}_s \cdot (\bar{\boldsymbol{u}}_s \bar{\Gamma}) = D_s \bar{\nabla}_s^2 \bar{\Gamma}, \tag{2.11}$$

where $D_s$ denotes the surface diffusivity of the surfactants, and $\bar{\boldsymbol{u}}_s$ denotes the fluid velocity on the droplet surface.

### 2.5. *Non-dimensional form of governing equations and boundary conditions*

Now, we apply the following non-dimensional scheme to the above set of governing equations and boundary conditions to obtain the relevant dimensionless form: $r = \bar{r}/a$, $\boldsymbol{u} = \bar{\boldsymbol{u}}/\bar{V}_c$, $T = (\bar{T} - \bar{T}_o)/|\bar{G}|a$, $\Gamma = \bar{\Gamma}/\bar{\Gamma}_{eq}$, $\sigma = \bar{\sigma}/\bar{\sigma}_o$, $p = \bar{p}/(\mu_e \bar{V}_c a)$, and $\boldsymbol{\tau} = \bar{\boldsymbol{\tau}}/(\mu_e \bar{V}_c/a)$. The various material ratios that appear are: viscosity ratio $\lambda = \mu_i/\mu_e$, and conductivity ratio $\delta = k_i/k_e$. On the other hand, different non-dimensional numbers that appear are: surface Péclet number $Pe_s = \bar{V}_c a/D_s$ (the ratio of the strength of the advection of the surfactant as compared to the diffusion of the same at the droplet interface), surfactant Marangoni number $Ma_\Gamma = \bar{\Gamma}_{eq} R_g \bar{T}_o/\mu_e \bar{V}_c$ (the relative strength of surfactant-induced interfacial-tension-driven Marangoni flow to that of the imposed Poiseuille flow), and thermal Marangoni number $Ma_T = \beta |\bar{G}| a/\mu_e \bar{V}_c$ (the ratio of thermally induced interfacial-tension-driven Marangoni flow and the imposed Poiseuille flow).

Imposing the above-mentioned scales, we obtained the non-dimensional form of the Laplace equation which governs the thermal problem as

$$\left.\begin{aligned} \nabla^2 T_i = 0, \\ \nabla^2 T_e = 0, \end{aligned}\right\} \tag{2.12}$$

which are subject to the following boundary conditions:

$$\left.\begin{aligned} \text{as } r \to \infty, \quad T_e = \zeta r \cos\theta, \\ T_i \text{ is bounded at } r = 0, \\ \text{at } r = 1, \quad T_i = T_e, \\ \text{at } r = 1, \quad \delta \frac{\partial T_i}{\partial r} = \frac{\partial T_e}{\partial r}. \end{aligned}\right\} \tag{2.13}$$

The factor $\zeta = \bar{G}/|\bar{G}|$ signifies the direction of the imposed temperature gradient. The imposed temperature increases (or decreases) in the direction of the imposed Poiseuille

flow for $\zeta = 1$ (or $\zeta = -1$). The flow problem is governed by the non-dimensional equations

$$\left.\begin{aligned} -\nabla p_i + \lambda \nabla^2 \boldsymbol{u}_i = \boldsymbol{0}, \quad \nabla \cdot \boldsymbol{u}_i = 0, \\ -\nabla p_e + \nabla^2 \boldsymbol{u}_e = \boldsymbol{0}, \quad \nabla \cdot \boldsymbol{u}_e = 0, \end{aligned}\right\} \tag{2.14}$$

which are subject to the following boundary conditions:

$$\left.\begin{aligned} \text{at } r \to \infty, \quad (\boldsymbol{u}_e, p_e) = (\boldsymbol{V}_\infty - \boldsymbol{U}, p_\infty), \\ \boldsymbol{u}_i \text{ is bounded at } r = 0, \\ \text{at } r = 1, \quad \boldsymbol{u}_i \cdot \boldsymbol{e}_r = \boldsymbol{u}_e \cdot \boldsymbol{e}_r = 0, \\ \text{at } r = 1, \quad \boldsymbol{u}_i = \boldsymbol{u}_e, \\ \text{at } r = 1, \quad (\boldsymbol{\tau}_e \cdot \boldsymbol{e}_r - \boldsymbol{\tau}_i \cdot \boldsymbol{e}_r) \cdot (\boldsymbol{I} - \boldsymbol{e}_r \boldsymbol{e}_r) = Ma_\Gamma \nabla_s \Gamma + Ma_T \nabla_s T_s. \end{aligned}\right\} \tag{2.15}$$

The last boundary condition (tangential stress balance) is obtained by substituting the dimensionless form of interfacial tension as

$$\sigma = 1 - Ca(Ma_T T + Ma_\Gamma \Gamma). \tag{2.16}$$

The surfactant transport equation, when non-dimensionalized, takes the form

$$Pe_s \nabla_s \cdot (\boldsymbol{u}_s \Gamma) = \nabla_s^2 \Gamma. \tag{2.17}$$

In addition to this, the surfactant concentration should also satisfy the following constraint to conserve the total mass of the surfactants on the droplet surface in the following form:

$$\int_{\varphi=0}^{2\pi} \int_{\theta=0}^{\pi} \Gamma(\theta, \varphi) \sin\theta \, \mathrm{d}\theta \, \mathrm{d}\varphi = 4\pi. \tag{2.18}$$

A closer look into (2.17) reveals the nonlinearity in the surfactant convection term. This makes the flow and surfactant transport coupled, due to which it is impossible to obtain an analytical solution for arbitrary values of $Pe_s$. Depending on the type of surfactant chosen, $Pe_s$ and $Ma_\Gamma$ can vary over a wide range. With $D_s = 10^{-11}$–$10^{-8}$ m$^2$ s$^{-1}$ and $\bar{\Gamma}_{eq} = 10^{-10}$–$10^{-6}$ mole m$^{-2}$ (Young *et al.* 1959; Stebe, Lin & Maldarelli 1991), the range of variation of $Pe_s$ is 0.1–100 and that for $Ma_\Gamma$ is 0.05–100. Towards making an analytical treatment, we focus on the following two regimes (Hanna & Vlahovska 2010; Pak *et al.* 2014): (i) $Pe_s \ll 1$ which signifies that the surface diffusion dominates the surfactant transport, and (ii) $Pe_s \to \infty$ which signifies that the surface convection governs the surfactant transport. The first limit represents the physical situation of large surface diffusivity of surfactants, while the second limit represents the physical situation of negligible surface diffusivity of surfactants (Kim & Subramanian 1989*a*; Vlahovska, Loewenberg & Blawzdziewicz 2005; Vlahovska *et al.* 2009).

## 3. Asymptotic solution

### 3.1. *Representation of field variables in terms of spherical harmonics*

As the temperature fields inside and outside the droplet satisfy the Laplace equation, we can represent them in terms of spherical solid harmonics as (Choudhuri

& Raja Sekhar 2013)

$$\left.\begin{aligned} T_i &= \sum_{n=0}^{\infty}\sum_{m=0}^{n}[a_{n,m}r^n\cos(m\varphi)+\hat{a}_{n,m}r^n\sin(m\varphi)]P_{n,m}(\cos\theta),\\ T_e &= \zeta r P_{1,0}(\cos\theta)\\ &\quad+\sum_{n=0}^{\infty}\sum_{m=0}^{n}[b_{-n-1,m}r^{-n-1}\cos(m\varphi)+\hat{b}_{-n-1,m}r^{-n-1}\sin(m\varphi)]P_{n,m}(\cos\theta), \end{aligned}\right\} \tag{3.1}$$

where $P_{n,m}(\cos\theta)$ is the associated Legendre polynomial of degree $n$ and order $m$. The temperature field inside the droplet ($T_i$) is constructed by linearly combining the growing spherical solid harmonics, which automatically satisfies the boundedness of $T_i$ at $r=0$. On the other hand, the temperature field outside the droplet ($T_e$) is constructed by linearly combining the far-field temperature field $T_\infty=\zeta r P_{1,0}(\cos\theta)$ and the decaying spherical solid harmonics, which automatically satisfies the boundedness of $T_e$ as $r\to\infty$. In (3.1), $a_{n,m}$, $\hat{a}_{n,m}$, $b_{-n-1,m}$ and $\hat{b}_{-n-1,m}$ are the unknown coefficients of the spherical solid harmonics, which will be obtained by using the remaining boundary conditions (continuity of temperature and heat flux across the droplet interface). The surface temperature ($T_s$) can be expressed as

$$T_s=\sum_{n=0}^{\infty}\sum_{m=0}^{n}[T_{n,m}\cos(m\varphi)+\hat{T}_{n,m}\sin(m\varphi)]P_{n,m}(\cos\theta), \tag{3.2}$$

where $T_{n,m}$ and $\hat{T}_{n,m}$ are the coefficients of the spherical surface harmonics. Similarly, the surfactant concentration $\Gamma$ can be represented in terms of spherical surface harmonics as (Haber & Hetsroni 1972; Pak *et al.* 2014)

$$\Gamma=\sum_{n=0}^{\infty}\sum_{m=0}^{n}[\Gamma_{n,m}\cos(m\varphi)+\hat{\Gamma}_{n,m}\sin(m\varphi)]P_{n,m}(\cos\theta), \tag{3.3}$$

where $\Gamma_{n,m}$ and $\hat{\Gamma}_{n,m}$ will be obtained by solving the surfactant transport equation.

As the velocity and pressure fields inside the droplet satisfy the Stokes and continuity equations, we can represent them in terms of the growing spherical solid harmonics using Lamb's general solution as (Haber & Hetsroni 1972)

$$\left.\begin{aligned} \boldsymbol{u}_i &= \sum_{n=1}^{\infty}\left[\nabla\times(\boldsymbol{r}\chi_n)+\nabla\Phi_n+\frac{n+3}{2(n+1)(2n+3)\lambda}r^2\nabla p_n-\frac{n}{(n+1)(2n+3)\lambda}\boldsymbol{r}p_n\right],\\ p_i &= \sum_{n=0}^{\infty}p_n, \end{aligned}\right\} \tag{3.4}$$

where $p_n$, $\Phi_n$ and $\chi_n$ are the growing spherical solid harmonics of the form

$$\left.\begin{aligned} p_n &= \lambda r^n\sum_{m=0}^{n}[A_{n,m}\cos(m\varphi)+\hat{A}_{n,m}\sin(m\varphi)]P_{n,m}(\cos\theta),\\ \Phi_n &= r^n\sum_{m=0}^{n}[B_{n,m}\cos(m\varphi)+\hat{B}_{n,m}\sin(m\varphi)]P_{n,m}(\cos\theta),\\ \chi_n &= r^n\sum_{m=0}^{n}[C_{n,m}\cos(m\varphi)+\hat{C}_{n,m}\sin(m\varphi)]P_{n,m}(\cos\theta). \end{aligned}\right\} \tag{3.5}$$

Similarly, the velocity and pressure fields outside the droplet can be represented in terms of the far-field velocity field and the decaying spherical solid harmonics using Lamb's solution as (Haber & Hetsroni 1972)

$$\left.\begin{aligned} \boldsymbol{u}_e &= (\boldsymbol{V}_\infty - \boldsymbol{U}) + \sum_{n=1}^{\infty}\left[\nabla\times(\boldsymbol{r}\chi_{-n-1}) + \nabla\Phi_{-n-1}\right. \\ &\quad \left. - \frac{n-2}{2n(2n-1)}r^2\nabla p_{-n-1} + \frac{n+1}{n(2n-1)}\boldsymbol{r}p_{-n-1}\right], \\ p_e &= p_\infty + \sum_{n=0}^{\infty} p_{-n-1}, \end{aligned}\right\} \tag{3.6}$$

where $p_{-n-1}$, $\Phi_{-n-1}$ and $\chi_{-n-1}$ are the decaying spherical solid harmonics of the form

$$\left.\begin{aligned} p_{-n-1} &= r^{-n-1}\sum_{m=0}^{n}[A_{-n-1,m}\cos(m\varphi) + \hat{A}_{-n-1,m}\sin(m\varphi)]P_{n,m}(\cos\theta), \\ \Phi_{-n-1} &= r^{-n-1}\sum_{m=0}^{n}[B_{-n-1,m}\cos(m\varphi) + \hat{B}_{-n-1,m}\sin(m\varphi)]P_{n,m}(\cos\theta), \\ \chi_{-n-1} &= r^{-n-1}\sum_{m=0}^{n}[C_{-n-1,m}\cos(m\varphi) + \hat{C}_{-n-1,m}\sin(m\varphi)]P_{n,m}(\cos\theta). \end{aligned}\right\} \tag{3.7}$$

The unknown coefficients $A_{n,m}$, $B_{n,m}$, $C_{n,m}$, $\hat{A}_{n,m}$, $\hat{B}_{n,m}$, $\hat{C}_{n,m}$, $A_{-n-1,m}$, $B_{-n-1,m}$, $C_{-n-1,m}$, $\hat{A}_{-n-1,m}$, $\hat{B}_{-n-1,m}$ and $\hat{C}_{-n-1,m}$ will be obtained by using the remaining boundary conditions (normal velocity, tangential velocity and tangential stress conditions).

### 3.2. *Solution for* $Pe_s \ll 1$

Irrespective of the value of $Pe_s$, the thermal problem is independent of the flow field and surfactant concentration. So, we obtain the solution for the temperature field inside and outside the droplet in the following form:

$$\left.\begin{aligned} T_i &= \zeta\left(\frac{3}{\delta+2}\right)rP_{1,0}(\cos\theta), \\ T_e &= \zeta\left[r + \left(\frac{1-\delta}{2+\delta}\right)\frac{1}{r^2}\right]P_{1,0}(\cos\theta). \end{aligned}\right\} \tag{3.8}$$

The surface temperature is obtained as $T_s = [3\zeta/(\delta+2)]P_{1,0}(\cos\theta)$, which gives the only one non-zero coefficient of surface harmonics in $T_s$ as $T_{1,0} = 3\zeta/(\delta+2)$.

In the low-$Pe_s$ limit, we use the following regular perturbation expansion for any dependent variable $\psi$ (Pak *et al.* 2014; Sekhar, Sharanya & Rohde 2016):

$$\psi = \psi^{(0)} + Pe_s\psi^{(Pe_s)} + Pe_s^2\psi^{(Pe_s^2)} + O(Pe_s^3), \tag{3.9}$$

where $\psi^{(0)}$ represents the leading-order term for $Pe_s = 0$, while $\psi^{(Pe_s)}$ and $\psi^{(Pe_s^2)}$ represent higher-order contributions for $Pe_s \ll 1$. Substituting this expansion in (2.17), we obtain the governing equation for surfactant concentration as (Pak *et al.* 2014)

$$\text{leading-order:} \quad \nabla^2\Gamma^{(0)} = 0, \tag{3.10}$$

$$O(Pe_s): \quad \nabla^2 \Gamma^{(Pe_s)} = \boldsymbol{\nabla} \cdot (\boldsymbol{u}_s^{(0)} \Gamma^{(0)}), \tag{3.11}$$

$$O(Pe_s^2): \quad \nabla^2 \Gamma^{(Pe_s^2)} = \boldsymbol{\nabla} \cdot (\boldsymbol{u}_s^{(0)} \Gamma^{(Pe_s)} + \boldsymbol{u}_s^{(Pe_s)} \Gamma^{(0)}). \tag{3.12}$$

A closer look into (3.10)–(3.12) reveals that at each order of perturbation the surfactant concentration is independent of the flow field (or surface velocity) at that order. So, we can solve for the surfactant concentration first, and then solve for flow field and droplet velocity.

To obtain the leading-order surfactant concentration (which is governed by (3.10)), we substitute $\Gamma^{(0)}(\theta, \varphi)$ in terms of surface harmonics (3.3) in (3.10). The distribution of $\Gamma^{(0)}$ which satisfies the mass conservation is obtained (by using the orthogonality of the associated Legendre polynomials and (2.18)) as

$$\Gamma^{(0)} = 1, \tag{3.13}$$

which gives the only one non-zero coefficient of surface harmonics as $\Gamma_{0,0}^{(0)} = 1$. We can obtain the leading-order velocity and pressure fields by substituting (3.4)–(3.7) in the boundary conditions (refer to appendix A for detailed expressions). To obtain the droplet velocity, we use the force-free condition. The total force acting on the droplet consists of the hydrodynamic force induced by the pressure and viscous stresses ($\boldsymbol{F}_H^{(0)}$) and the buoyancy force ($\boldsymbol{F}_B$) due to the difference in density in either of the phases. At steady state the force-free condition is given by (Happel & Brenner 1981)

$$\boldsymbol{F}_H^{(0)} + \boldsymbol{F}_B = 0 \quad \Rightarrow \quad \int_{\varphi=0}^{2\pi} \int_{\theta=0}^{\pi} (\boldsymbol{\tau}_e^{(0)} \cdot \boldsymbol{e}_r) \sin\theta \, \mathrm{d}\theta \, \mathrm{d}\varphi + \left( \frac{4\pi \xi Bo}{3Ca} \right) \boldsymbol{e}_z = 0, \tag{3.14}$$

where $Bo = |\rho_i - \rho_e| g a^2 / \bar{\sigma}_o$ is the Bond number, which signifies the relative strength of the buoyancy force as compared to the interfacial tension force. The parameter $Bo/Ca = |\rho_i - \rho_e| g a^2 / \mu_e \bar{V}_c$, on the other hand, indicates the relative significance of the buoyancy forces with respect to the viscous forces. In our present analysis we thus deal with the parameter $Bo/Ca$ instead of $Bo$, as the former has a greater impact. For the neutrally buoyant system at 32 °C according to the property values given by Hähnel *et al.* (1989), we have $Bo/Ca = 9.85 \times 10^{-4} \approx 0$. The factor '$\xi$' decides the denser fluid among the droplet and the suspending phase. That is, $\xi = 1$ indicates that the droplet phase is denser as compared to the carrier phase ($\rho_i > \rho_e$), while $\xi = -1$ denotes that the suspending phase is denser ($\rho_i < \rho_e$). For the case of a methanol–silicone oil system we have $\xi = -1$ and the magnitude of $Bo/Ca$ is 0.8363 according to the property values for silicone oil as used in the experimental work done by Nallani & Subramanian (1993). However, the value of $Bo/Ca$ usually varies between 0.1 and 3, depending on the type of silicone oil chosen. If we consider a separate system with silicone oil as the droplet phase and methanol as the suspending phase, keeping the property values for either of the phases intact, then the magnitude of $Bo/Ca$ remains the same although $\xi = 1$. The other dimensionless governing parameters ($Ca$, $Re$, $Pe_s$ and $Ma_\Gamma$) still fall in a regime that satisfies the major assumptions made in this study. The hydrodynamic force acting on the droplet can be expressed in terms of spherical harmonics in the following form (Happel & Brenner 1981):

$$\boldsymbol{F}_H^{(0)} = \int_{\varphi=0}^{2\pi} \int_{\theta=0}^{\pi} (\boldsymbol{\tau}_e^{(0)} \cdot \boldsymbol{e}_r) \sin\theta \, \mathrm{d}\theta \, \mathrm{d}\varphi = -4\pi \boldsymbol{\nabla} (r^3 p_{-2}^{(0)}), \tag{3.15}$$

where the spherical solid harmonics $p_{-2}^{(0)}$ is of the form

$$p_{-2}^{(0)} = r^{-3}[A_{-2,0}^{(0)} P_{2,0}(\cos\theta) + A_{-2,1}^{(0)} \cos\phi P_{2,1}(\cos\theta) + \hat{A}_{-2,1}^{(0)} \sin\phi P_{2,1}(\cos\theta)]. \tag{3.16}$$

Substituting $A_{-2,0}^{(0)}$, $A_{-2,1}^{(0)}$ and $\hat{A}_{-2,1}^{(0)}$ (expressions are given in appendix A), we obtain the components of droplet velocity in the axial (along $z$) and cross-stream (along $x$ and $y$) directions as

$$\left.\begin{aligned} U_z^{(0)} = \Bigg[ &\underbrace{\frac{2}{3}\left(\xi\frac{Bo}{Ca}\right)\left(\frac{1+\lambda}{3\lambda+2}\right)}_{\textit{Effect of buoyancy}} + \underbrace{\left\{1-\left(\frac{e}{R}\right)^2 - \left(\frac{5\lambda}{3\lambda+2}\right)\frac{2}{5R^2}\right\}}_{\textit{Effect of Poiseuille flow}} \\ &+ \underbrace{\frac{2\zeta Ma_T}{(3\lambda+2)(\delta+2)}}_{\textit{Effect of temperature gradient}}\Bigg], \\ U_x^{(0)} = U_y^{(0)} = 0. \end{aligned}\right\} \tag{3.17}$$

The first term in $U_z^{(0)}$ indicates the sole effect of the buoyancy force on the leading-order axial velocity of the droplet, the second bracketed term is due to imposed Poiseuille flow, while the third term is the droplet velocity solely due to a linearly varying temperature field. Accordingly, the leading-order droplet velocity is not affected by the presence of surfactants. This is due to the fact that the leading-order surfactant-induced Marangoni stress vanishes, $\nabla_s \Gamma^{(0)} = \mathbf{0}$, for a uniform distribution of surfactants. The leading-order surface velocity is obtained as

$$\begin{aligned} \boldsymbol{u}_s^{(0)} = &\left\{\frac{1}{3}\left(\xi\frac{Bo}{Ca}\right)\frac{\sin\theta}{3\lambda+2} + \frac{3\sin\theta Ma_T\zeta}{(\delta+2)(3\lambda+2)} + \frac{(\lambda+2\sin^2\theta)e\cos\varphi}{R^2(\lambda+1)} + \frac{5\sin^3\theta}{4R^2(\lambda+1)}\right. \\ &\left. - \frac{\lambda\sin\theta}{R^2(3\lambda+2)(\lambda+1)}\right\}\boldsymbol{e}_\theta - \frac{e\lambda\sin\varphi\cos\theta}{R^2(\lambda+1)}\boldsymbol{e}_\varphi. \end{aligned} \tag{3.18}$$

Now, we substitute $\Gamma^{(0)}$ and $\boldsymbol{u}_s^{(0)}$ in (3.11) and use the surface harmonic representation (3.3) for the $O(Pe_s)$ surfactant concentration. The $O(Pe_s)$ surfactant concentration is obtained as

$$\Gamma^{(Pe_s)} = \Gamma_{1,0}^{(Pe_s)} P_{1,0}(\cos\theta) + \Gamma_{2,1}^{(Pe_s)} \cos\varphi P_{2,1}(\cos\theta) + \Gamma_{3,0}^{(Pe_s)} P_{3,0}(\cos\theta), \tag{3.19}$$

where the coefficients of the surface harmonics are obtained as

$$\left.\begin{aligned} \Gamma_{1,0}^{(Pe_s)} = -\frac{1}{3\lambda+2}\left\{\frac{\xi Bo}{3Ca} + \left(\frac{3Ma_T\zeta}{\delta+2} + \frac{2}{R^2}\right)\right\}, \quad \Gamma_{2,1}^{(Pe_s)} = -\frac{e}{3R^2(\lambda+1)}, \\ \Gamma_{3,0}^{(Pe_s)} = \frac{1}{6R^2(\lambda+1)}. \end{aligned}\right\} \tag{3.20}$$

Similar to the leading-order calculation (except there is no thermocapillary-induced Marangoni stress at the droplet interface at $O(Pe_s)$), we obtain the $O(Pe_s)$ velocity

and pressure fields (refer to appendix A for detailed expressions). The $O(Pe_s)$ droplet velocity is obtained from the force-free condition, which is now given by

$$\boldsymbol{F}_H^{(Pe_s)} = -4\pi\nabla(r^3 p_{-2}^{(Pe_s)}) = \boldsymbol{0}. \tag{3.21}$$

The expression of the different components of the $O(Pe_s)$ droplet migration velocity is given by

$$\left.\begin{aligned} U_z^{(Pe_s)} &= -\frac{Ma_\Gamma}{(3\lambda+2)^2}\left[\frac{2\xi}{9}\frac{Bo}{Ca} + \left\{\frac{Ma_T\zeta}{(\delta+2)} + \frac{2}{3R^2}\right\}\right], \\ U_x^{(Pe_s)} &= U_y^{(Pe_s)} = 0. \end{aligned}\right\} \tag{3.22}$$

It is evident from the above expression that the surfactant-induced Marangoni stress affects the axial droplet velocity at $O(Pe_s)$.

The $O(Pe_s)$ surface velocity is obtained as

$$\begin{aligned} \boldsymbol{u}_s^{(Pe_s)} = Ma_\Gamma \Bigg\{ &-\frac{\xi}{3}\frac{Bo}{Ca}\frac{\sin\theta}{(3\lambda+2)^2} - \frac{3\sin\theta Ma_T\zeta}{(\delta+2)(3\lambda+2)^2} + \frac{e\cos(2\theta)}{5R^2(\lambda+1)^2}\cos\varphi \\ &- \frac{5\sin^3\theta}{28R^2(\lambda+1)^2} - \frac{4(5\lambda^2+16\lambda+8)\sin\theta}{28R^2(3\lambda+2)^2(\lambda+1)^2}\Bigg\}\boldsymbol{e}_\theta - \frac{Ma_\Gamma e\sin\varphi\cos\theta}{5R^2(\lambda+1)^2}\boldsymbol{e}_\varphi. \end{aligned} \tag{3.23}$$

Now, we substitute $\Gamma^{(0)}$, $\boldsymbol{u}_s^{(0)}$, $\Gamma^{(Pe_s)}$ and $\boldsymbol{u}_s^{(Pe_s)}$ in (3.12) and use the surface harmonic representation (refer to (3.3)) for the $O(Pe_s^2)$ surfactant concentration. The $O(Pe_s^2)$ surfactant concentration is obtained as

$$\begin{aligned} \Gamma^{(Pe_s^2)} = \Bigg\{ &\Gamma_{1,0}^{(Pe_s^2)} P_{1,0}(\cos\theta) + \Gamma_{1,1}^{(Pe_s^2)}\cos\varphi P_{1,1}(\cos\theta) \\ &+ \Gamma_{2,0}^{(Pe_s^2)} P_{2,0}(\cos\theta) + \Gamma_{2,1}^{(Pe_s^2)}\cos\varphi P_{2,1}(\cos\theta) \\ &+ \Gamma_{2,2}^{(Pe_s^2)}\cos(2\varphi) P_{2,2}(\cos\theta) + \Gamma_{3,0}^{(Pe_s^2)} P_{3,0}(\cos\theta) + \Gamma_{3,1}^{(Pe_s^2)}\cos\varphi P_{3,1}(\cos\theta), \end{aligned} \tag{3.24}$$

where the coefficients of surface harmonics are mentioned in appendix B. Similar to the $O(Pe_s)$ calculation, we obtain the $O(Pe_s^2)$ velocity and pressure fields (refer to appendix A for detail expressions), and we obtain the droplet velocity using the force-free condition as

$$\left.\begin{aligned} U_z^{(Pe_s^2)} &= \frac{2Ma_\Gamma^2}{3(3\lambda+2)^3}\left[\frac{\xi Bo}{3Ca} + \frac{2}{R^2} + \frac{3Ma_T\zeta}{(2+\delta)}\right], \\ U_x^{(Pe_s^2)} &= -\frac{Ma_\Gamma e}{5(3\lambda+2)^2(\lambda+1)R^2}\left[(5\lambda+3)\left\{\frac{\xi Bo}{9Ca} + \frac{Ma_T\zeta}{(2+\delta)}\right\} + \frac{70\lambda^2+109\lambda+40}{21(\lambda+1)}\right], \\ U_y^{(Pe_s^2)} &= 0. \end{aligned}\right\} \tag{3.25}$$

It is evident from the above expression that the surfactant-induced Marangoni stress not only affects the axial velocity but also induces a cross-stream migration velocity of the droplet along $x$. It is interesting to note that though the temperature gradient and gravity are acting along the axial direction, both these effects induce the drop motion in the cross-stream direction.

### 3.3. *Solution for* $Pe_s \to \infty$

In the high-$Pe_s$ limit, the surfactant transport equation simplifies to (Hanna & Vlahovska 2010)

$$\nabla_s \cdot (\boldsymbol{u}_s \Gamma) = 0, \tag{3.26}$$

which is still a nonlinear equation. Following Hanna & Vlahovska (2010), we consider the limiting situation of $Ma_\Gamma \gg 1$. We expand any dependent variable $\psi$ (except the surfactant concentration $\Gamma$) in the following asymptotic form (Hanna & Vlahovska 2010; Schwalbe *et al.* 2011):

$$\psi = \psi^{(0)} + Ma_\Gamma^{-1}\psi^{(Ma_\Gamma^{-1})} + O(Ma_\Gamma^{-2}), \tag{3.27}$$

where $\psi^{(0)}$ represents the leading-order term for $Ma_\Gamma \to \infty$, and $\psi^{(Ma_\Gamma^{-1})}$ represents the higher order correction for $Ma_\Gamma^{-1} \ll 1$. The surfactant concentration is expanded in the following form (Hanna & Vlahovska 2010; Schwalbe *et al.* 2011):

$$\Gamma = 1 + Ma_\Gamma^{-1}\Gamma^{(0)} + Ma_\Gamma^{-2}\Gamma^{(Ma_\Gamma^{-1})} + O(Ma_\Gamma^{-3}). \tag{3.28}$$

Substituting (3.27) and (3.28) in (3.26), we obtain the governing equation for surfactant concentration at different orders of perturbation as

$$\text{leading-order:} \quad \nabla \cdot \boldsymbol{u}_s^{(0)} = 0, \tag{3.29}$$

$$O(Ma_\Gamma^{-1}): \quad \nabla \cdot (\boldsymbol{u}_s^{(0)}\Gamma^{(0)} + \boldsymbol{u}_s^{(Ma_\Gamma^{-1})}) = 0. \tag{3.30}$$

The tangential stress balance at the droplet surface ($r = 1$) can be obtained as

$$\text{leading-order:} \quad (\boldsymbol{\tau}_e^{(0)} \cdot \boldsymbol{e}_r - \boldsymbol{\tau}_i^{(0)} \cdot \boldsymbol{e}_r) \cdot (\boldsymbol{I} - \boldsymbol{e}_r\boldsymbol{e}_r) = \nabla_s \Gamma^{(0)} + Ma_T \nabla_s T_s \tag{3.31}$$

$$O(Ma_\Gamma^{-1}): \quad (\boldsymbol{\tau}_e^{(Ma_\Gamma^{-1})} \cdot \boldsymbol{e}_r - \boldsymbol{\tau}_i^{(Ma_\Gamma^{-1})} \cdot \boldsymbol{e}_r) \cdot (\boldsymbol{I} - \boldsymbol{e}_r\boldsymbol{e}_r) = \nabla_s \Gamma^{(Ma_\Gamma^{-1})}. \tag{3.32}$$

A closer look into (3.29)–(3.32) reveals that the surfactant concentration and flow field have to be obtained simultaneously. Similar to the low-$Pe_s$ limit, the temperature field is independent of the flow field and surfactant concentration. So, the solution for the temperature field will be the same as given in (3.8). Now, we substitute the velocity and pressure fields given in (3.4)–(3.7) in the boundary conditions (refer to appendix C for detailed expressions for different spherical harmonics present in the flow field). The leading-order surfactant concentration and surface velocity are obtained as

$$\left.\begin{aligned} \Gamma^{(0)} &= -\frac{\xi Bo}{3Ca}\cos\theta - \frac{\cos\theta}{12(\delta+2)} \\ &\quad \times \left[36 Ma_T \zeta + \frac{5(\delta+2)}{R^2}(9 + 12e\cos\varphi\sin\theta - 7\cos^2\theta)\right], \\ \boldsymbol{u}_s^{(0)} &= \left(\frac{e\cos\varphi}{R^2}\right)\boldsymbol{e}_\theta - \frac{e\sin\varphi\cos\theta}{R^2}\boldsymbol{e}_\varphi. \end{aligned}\right\} \tag{3.33}$$

Similar to the previous limiting case, the force-free condition is given by (3.15), which gives the leading-order droplet velocity as

$$U_z^{(0)} = \frac{2\xi Bo}{9Ca} + 1 - \frac{2}{3R^2} - \left(\frac{e}{R}\right)^2, \quad U_x^{(0)} = U_y^{(0)} = 0. \tag{3.34a,b}$$

It is evident from the above expression that the surfactant-induced Marangoni stress leads to motion of the droplet at the speed of a solid particle. Thermocapillarity has no effect on the droplet speed at the leading-order approximation.

The $O(Ma_\Gamma^{-1})$ surfactant concentration is obtained as

$$\Gamma^{(Ma_\Gamma^{-1})} = \begin{bmatrix} \Gamma_{1,1}^{(Ma_\Gamma^{-1})}\cos\varphi P_{1,1}(\cos\theta) + \Gamma_{2,0}^{(Ma_\Gamma^{-1})} P_{2,0}(\cos\theta) \\ + \Gamma_{2,2}^{(Ma_\Gamma^{-1})}\cos 2\varphi P_{2,2}(\cos\theta) + \Gamma_{3,1}^{(Ma_\Gamma^{-1})}\cos\varphi P_{3,1}(\cos\theta) \end{bmatrix}, \tag{3.35}$$

where the coefficients of the surface harmonics are of the form

$$\left.\begin{aligned} \Gamma_{1,1}^{(Ma_\Gamma^{-1})} &= -\frac{\xi Bo}{6Ca}\frac{e(3\lambda+2)}{R^2} - \frac{3}{2}\frac{e(4+3Ma_T\zeta R^2+2\delta)(\lambda+1)}{R^4(\delta+2)}, \\ \Gamma_{0,2}^{(Ma_\Gamma^{-1})} &= \frac{25}{6}\frac{e^2(\lambda+1)}{R^4}, \quad \Gamma_{2,2}^{(Ma_\Gamma^{-1})} = -\frac{25}{36}\frac{e^2(\lambda+1)}{R^4}, \quad \Gamma_{3,1}^{(Ma_\Gamma^{-1})} = \frac{49}{72}\frac{e(\lambda+1)}{R^4}. \end{aligned}\right\} \tag{3.36}$$

The force-free condition gives the $O(Ma_\Gamma^{-1})$ droplet velocity as

$$U_z^{(Ma_\Gamma^{-1})} = U_y^{(Ma_\Gamma^{-1})} = 0, \quad U_x^{(Ma_\Gamma^{-1})} = -\frac{\xi Bo}{9Ca}\frac{e}{R^2} - \frac{e(4+3Ma_T\zeta R^2+2\delta)}{3R^4(\delta+2)}. \tag{3.37a,b}$$

Equation (3.37) shows that the surfactant-induced Marangoni stress induces a non-zero cross-stream migration of the droplet along $x$. Importantly, thermocapillarity and gravity affect the cross-stream velocity of the droplet at this order of approximation.

## 4. Results and discussion

We analyse the results for the following two special cases: (i) neutrally buoyant droplet ($\rho_i = \rho_e$) for which $Bo = 0$, and (ii) buoyant droplet ($\rho_i \neq \rho_e$) for which $Bo \neq 0$.

### 4.1. *Neutrally buoyant droplet* ($Bo = 0$)

#### 4.1.1. *Effect of Marangoni stress in the low-$Pe_s$ limit*

The main result of the present analysis is the velocity of a force-free surfactant-laden droplet in the combined presence of Poiseuille flow and a linearly varying temperature field. We have obtained the velocity of a neutrally buoyant droplet in the low-$Pe_s$ limit as

$$\begin{aligned} \boldsymbol{U} = & \left[\left\{1 - \left(\frac{e}{R}\right)^2 - \frac{2\lambda}{(3\lambda+2)R^2} + \frac{2\zeta Ma_T}{(3\lambda+2)(\delta+2)}\right\}\right. \\ & - Pe_s\left\{\frac{2Ma_\Gamma}{(3\lambda+2)^2}\left(\frac{Ma_T\zeta}{\delta+2} + \frac{2}{3R^2}\right)\right\} + Pe_s^2\left\{\frac{2Ma_\Gamma^2}{3(3\lambda+2)^3}\left(\frac{2}{R^2} + \frac{3Ma_T\zeta}{2+\delta}\right)\right\}\Bigg]\boldsymbol{e}_z \\ & - \left[Pe_s^2 Ma_\Gamma e\left\{\frac{Ma_T\zeta(5\lambda+3)}{5R^2(3\lambda+2)^2(\lambda+1)(2+\delta)} + \frac{70\lambda^2+109\lambda+40}{105R^4(3\lambda+2)^2(\lambda+1)^2}\right\}\right]\boldsymbol{e}_x \\ & + O(Pe_s^3). \end{aligned} \tag{4.1}$$

Substituting $Ma_T = 0$ in (4.1), we recover the velocity of a surfactant-laden droplet in isothermal Poiseuille flow in the low-$Pe_s$ limit which was previously obtained by Pak *et al.* (2014). Substituting $e = 0$ in (4.1), we obtain the axial

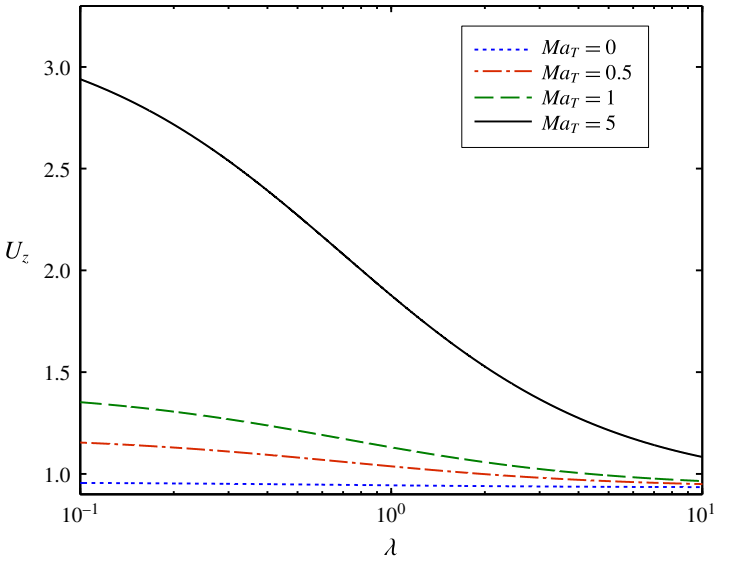


FIGURE 2. (Colour online) The variation of the axial droplet velocity ($U_z$) with the viscosity ratio ($\lambda$) for different values of $Ma_T$. Other parameters have the following values: $\zeta = 1$, $Ma_T = 1$, $Pe_s = 0.1$, $\delta = 0.1$, $e = 1$ and $R = 5$.

velocity of a surfactant-laden droplet in non-isothermal Poiseuille flow which was previously obtained by Das *et al.* (2017). A closer look into (4.1) reveals that the thermocapillary-induced Marangoni stress in the presence of surfactant-induced Marangoni stress alters both the axial and cross-stream velocities of the droplet.

Now, we investigate the effects of Marangoni stresses on the axial velocity of the droplet. Towards this, we first plot figure 2, which shows the variation of droplet velocity in the axial direction ($U_z$) with the viscosity ratio ($\lambda$) for the particular case in which the temperature increases in the direction of the Poiseuille flow (i.e. $\zeta = 1$). $Ma_T = 0$ represents the special case of a surfactant-laden droplet in an isothermal Poiseuille flow. When $Ma_T > 0$ figure 2 depicts a significant increase in magnitude of the axial droplet velocity. This is due to the fact that for $\zeta = 1$ the thermocapillary-induced Marangoni stress drives the droplet in the direction of the Poiseuille flow. The effect of Marangoni stress diminishes in the limit $\lambda \to \infty$, due to the fact that the droplet surface becomes more rigid and the interfacial tension plays no role in governing the hydrodynamics.

We next consider the special case of $\zeta = -1$, which signifies a decreasing temperature field in the imposed Poiseuille flow direction. Figure 3 shows the variation of droplet velocity in the axial direction ($U_z$) with the viscosity ratio ($\lambda$) for different values of $Ma_T$. In this case the thermocapillary-induced Marangoni stress acts to drive the droplet in the direction opposite to the Poiseuille flow. For smaller values of $Ma_T$ (e.g. $Ma_T = 0.5$), the effect of the imposed Poiseuille flow dominates and the droplet moves in the direction of the Poiseuille flow (i.e. $U_z > 0$). For larger values of $Ma_T$ (e.g. $Ma_T = 5$) the droplet moves in the direction of the Poiseuille flow (i.e. $U_z > 0$) for a larger viscosity ratio, while a low-viscosity droplet moves opposite to the Poiseuille flow (i.e. $U_z < 0$). For a given viscosity ratio ($\lambda$),

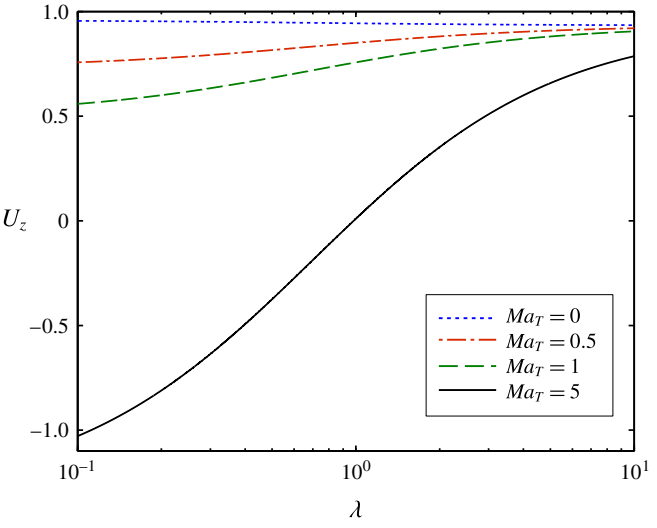


FIGURE 3. (Colour online) The variation of the axial droplet velocity ($U_z$) with the viscosity ratio ($\lambda$) for the special case of $\zeta = -1$. Other parameters have the following values: $Ma_\Gamma = 1$, $Pe_s = 0.1$, $\delta = 0.1$, $e = 1$ and $R = 5$.

we obtain a critical value of $Ma_T$ for which $U_z = 0$ in the following form:

$$Ma^*_{T,z} = \frac{[3(3\lambda+2)^2\{(R^2-e^2)(3\lambda+2)-2\lambda\} - 4Ma_\Gamma(3\lambda+2)Pe_s + 4Ma_\Gamma^2 Pe_s^2](\delta+2)}{6R^2\{(3\lambda+2)^2 - Ma_\Gamma(3\lambda+2)Pe_s + Ma_\Gamma^2 Pe_s^2\}}. \tag{4.2}$$

It is important to note that for $Ma_T < Ma^*_{T,z}$ the magnitude of axial droplet velocity decreases with increasing $Ma_T$, while the magnitude of axial droplet velocity increases with increasing $Ma_T$ for $Ma_T > Ma^*_{T,z}$.

Now, we investigate the effects of Marangoni stresses on the cross-stream velocity of the droplet. Towards this, we first plot figure 4, which shows the variation of droplet velocity in the cross-stream direction ($U_x$) with the viscosity ratio ($\lambda$) for the case in which the temperature increases in the direction of the Poiseuille flow (i.e. $\zeta = 1$). For isothermal Poiseuille flow (i.e. $Ma_T = 0$), Pak *et al.* (2014) obtained cross-stream motion of a surfactant-laden droplet. They have obtained that an eccentrically positioned droplet always moves towards the channel centreline (represented by negative values of $U_x$ in figure 4). Figure 4 depicts that in the presence of temperature variation (i.e. $Ma_T > 0$ with increasing temperature in the direction of the imposed Poiseuille flow), there is a significant increase in the magnitude of the cross-stream velocity (i.e. $|U_x|$). So the thermocapillary-induced Marangoni stress aids the surfactant-induced cross-stream migration of the droplet for $\zeta = 1$. The magnitude of the cross-stream velocity increases with increasing $Ma_T$ for low-viscosity droplets. Similar to axial velocity, the effect of $Ma_T$ (i.e. thermocapillary-induced Marangoni stress) on the cross-stream velocity of the droplet diminishes for a larger viscosity ratio (i.e. $\lambda \to \infty$).

We next consider the special case of $\zeta = -1$, which signifies a decreasing temperature field in the imposed Poiseuille flow direction. Figure 5 shows the variation of droplet velocity in the cross-stream direction ($U_x$) with the viscosity ratio ($\lambda$) for different values of $Ma_T$. In this case the thermocapillary-induced Marangoni stress

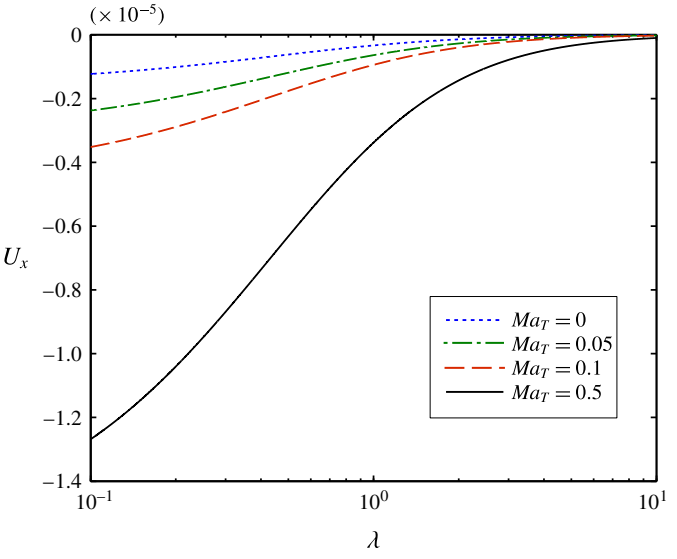


FIGURE 4. (Colour online) The variation of the cross-stream droplet velocity ($U_x$) with the viscosity ratio ($\lambda$) for different values of $Ma_T$. Other parameters have the following values: $\zeta = 1$, $Ma_\Gamma = 1$, $Pe_s = 0.1$, $\delta = 0.1$, $e = 1$ and $R = 5$.

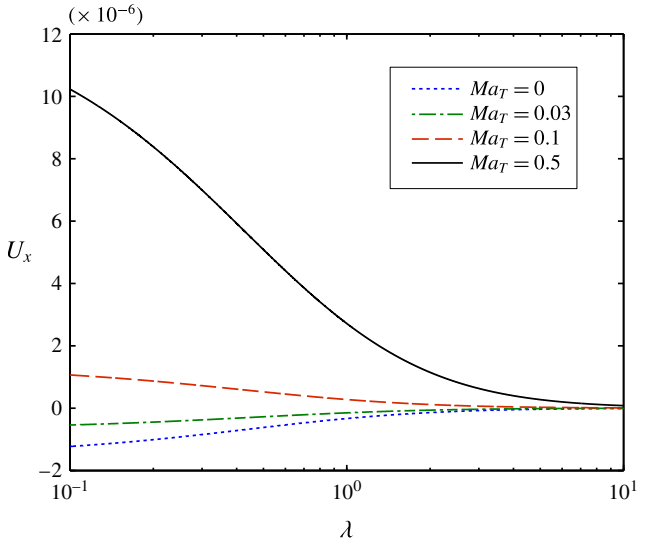


FIGURE 5. (Colour online) The variation of the cross-stream droplet velocity ($U_x$) with the viscosity ratio ($\lambda$) for different values of $Ma_T$. Other parameters have the following values: $\zeta = -1$, $Ma_\Gamma = 1$, $Pe_s = 0.1$, $\delta = 0.1$, $e = 1$ and $R = 5$.

not only alters the magnitude of the cross-stream migration velocity but also alters its direction. For smaller values of $Ma_T$ (e.g. $Ma_T = 0.03$) the droplet moves towards the channel centreline (i.e. $U_x < 0$). However, for larger values of $Ma_T$ (e.g. $Ma_T = 0.5$) the droplet moves away from the channel centreline (i.e. $U_x > 0$). One can find a

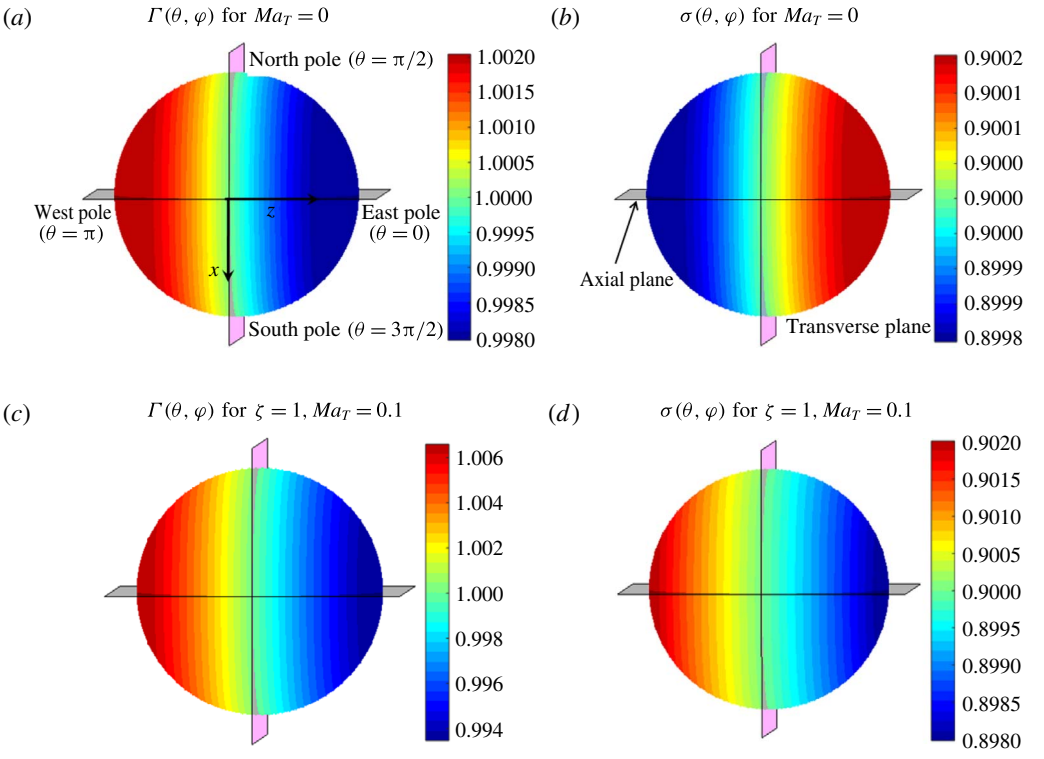


FIGURE 6. (Colour online) Surface plot showing the variation of the surfactant concentration for (*a*) $Ma_T = 0$, (*c*) $\zeta = 1$ and $Ma_T = 0.1$. Surface plot showing the variation of the interfacial tension for (*b*) $Ma_T = 0$, (*d*) $\zeta = 1$ and $Ma_T = 0.1$. Other parameters have the following values: $Ma_\Gamma = 5$, $Pe_s = 0.1$, $\delta = 0.1$, $\lambda = 0.1$, $e = 0$ and $R = 5$.

critical value of $Ma_T$ for which $U_x = 0$ in the following form:

$$Ma^*_{T,x} = \frac{(\delta + 2)(70\lambda^2 + 109\lambda + 40)}{21(5\lambda + 3)(\lambda + 1)R^2}. \tag{4.3}$$

It is important to note that for $Ma_T < Ma^*_{T,x}$ the magnitude of cross-stream velocity decreases with increasing $Ma_T$, while the magnitude of cross-stream velocity increases with increasing $Ma_T$ for $Ma_T > Ma^*_{T,x}$.

The physical reason for the change in magnitude and direction of the axial and cross-stream velocities of a surfactant-laden droplet in non-isothermal Poiseuille flow can be understood by looking into the distribution of surfactant concentration and interfacial tension on the droplet surface. Towards this, we first look into the case of a droplet located at the flow centreline (i.e. $e = 0$). Figure 6(*a*,*b*) depicts the distribution of $\Gamma(\theta, \varphi)$ and $\sigma(\theta, \varphi)$ for the particular case of $Ma_T = 0$ (i.e. isothermal Poiseuille flow). The imposed Poiseuille flow alters the surfactant distribution from its equilibrium value $\Gamma_{eq} = 1$. The surfactant concentration is less near the east pole as compared with the west pole, as depicted in figure 6(*a*). So, the altered surfactant distribution is asymmetric about the transverse plane. This distribution is due to the imposed Poiseuille flow, which drives the surfactants from the east pole to the west pole. The asymmetry in $\Gamma(\theta, \varphi)$ leads to an asymmetric distribution of $\sigma(\theta, \varphi)$ about the transverse plane, which is depicted in figure 6(*b*). Larger interfacial

tension near the east pole as compared with the west pole drives a surfactant-induced Marangoni flow from the west to the east pole, which leads to the generation of a hydrodynamic force in the axial direction opposite to the Poiseuille flow. This reduces the droplet speed in the axial direction as compared with the speed of a surfactant-free droplet. The distributions of $\Gamma(\theta, \varphi)$ and $\sigma(\theta, \varphi)$ remain symmetric about the axial plane, which results in no motion of the droplet in the cross-stream direction. The distributions of $\Gamma(\theta, \varphi)$ and $\sigma(\theta, \varphi)$ in non-isothermal Poiseuille flow (i.e. $Ma_T > 0$) for $\zeta = 1$ (i.e. increasing temperature in the direction of Poiseuille flow) are shown in figures 6(*c*) and 6(*d*), respectively. For $\zeta = 1$ the thermocapillary-induced Marangoni stress induces a flow at the droplet surface which runs from the east to west pole. This flow drives surfactants away from the east pole towards the west pole which leads to an increase in the asymmetry in $\Gamma(\theta, \varphi)$. Comparison of figures 6(*c*) with 6(*a*) reflects the increase in asymmetry in terms of an increase in $(\Gamma_{max} - \Gamma_{min})$. This surfactant distribution combined with the non-uniform temperature distribution leads to larger $\sigma(\theta, \varphi)$ near the west pole as compared with the east pole (refer to figure 6*d*), which is in sharp contrast to the case of $Ma_T = 0$ shown in figure 6(*b*). This is due to the fact that the east pole encounters relatively hot fluid (higher temperature means lower interfacial tension). This distribution of $\sigma(\theta, \varphi)$ drives a Marangoni flow from the east to the west pole which leads to motion of the droplet in the direction of the Poiseuille flow with an increased velocity as compared with $Ma_T = 0$.

Now, we consider the case of $\zeta = -1$ (i.e. decreasing temperature in the direction of Poiseuille flow) and $e = 0$. For $\zeta = -1$ the thermocapillary-induced Marangoni stress induces a flow at the droplet surface which runs from the west to east pole. This flow drives surfactants from the west to the east pole, while the imposed Poiseuille flow drives the surfactants in the opposite direction (i.e. from the east to the west pole). The final surfactant distribution is decided by the net surface velocity. For $Ma_T = 0.5$, the distributions of $\Gamma(\theta, \varphi)$ and $\sigma(\theta, \varphi)$ are shown in figures 7(*a*) and 7(*b*), respectively. Figure 7(*a*) depicts that the combined effect of thermocapillary-induced Marangoni stress and imposed Poiseuille flow leads to a larger surfactant concentration near the east pole as compared with the west pole. This surfactant distribution combined with the non-uniform temperature distribution leads to larger $\sigma(\theta, \varphi)$ near the east pole as compared with the west pole, as depicted in figure 7(*b*). This Marangoni stress induces a hydrodynamic force in the direction opposite to the Poiseuille flow. For $Ma_T = 0.5$ the Poiseuille flow dominates and the droplet moves in the direction of the Poiseuille flow, but with a decreased axial velocity of the droplet.

Now, we consider $Ma_T = 5$ and plot $\Gamma(\theta, \varphi)$ and $\sigma(\theta, \varphi)$ in figures 7(*c*) and 7(*d*), respectively. With larger $Ma_T$, the strong effect of thermocapillary-induced Marangoni stress leads to a significant increase (and decrease) in surfactant concentration near the east (and west) pole. Comparison between figure 7(*a*,*c*) reveals that $(\Gamma_{max} - \Gamma_{min})$ is much larger for $Ma_T = 5$. A similar increase in asymmetry is also reflected in figure 7(*d*) for $\sigma(\theta, \varphi)$. In this case the Marangoni stress dominates over the Poiseuille flow and the droplet moves in the direction opposite to the Poiseuille flow.

Interesting things happen for $e = 1$ (i.e. eccentrically located droplet). The distributions of $\Gamma(\theta, \varphi)$ and $\sigma(\theta, \varphi)$ in isothermal Poiseuille flow (i.e. $Ma_T = 0$) for $e = 1$ and $\zeta = 1$ are shown in figures 8(*a*) and 8(*b*), respectively. Figure 8(*a*) depicts that the surfactant concentration is maximum near the northwest pole and minimum near the northeast pole. So, now the distribution of $\Gamma(\theta, \varphi)$ is asymmetric about both the transverse and axial planes. The asymmetry about the axial plane is due to the asymmetric velocity field about the axial plane encountered by the

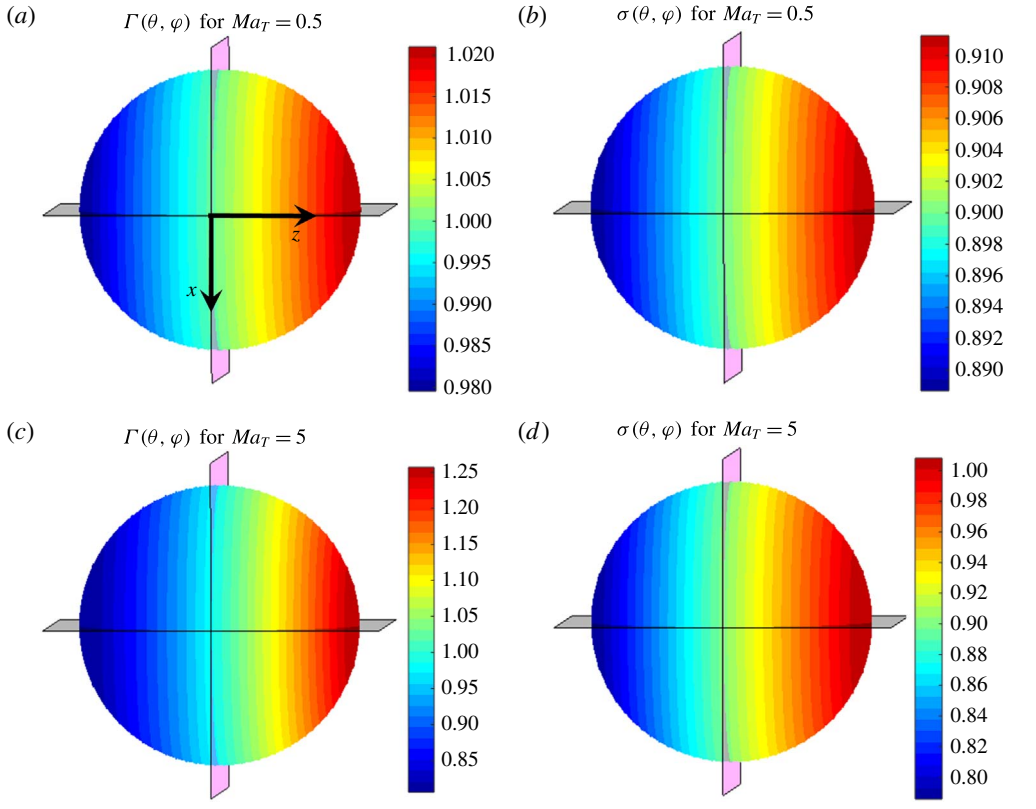


FIGURE 7. (Colour online) Surface plot showing the variation of the surfactant concentration for (*a*) $Ma_T = 0.5$, (*c*) $Ma_T = 5$. Surface plot showing the variation of the interfacial tension for (*b*) $Ma_T = 0.5$, (*d*) $Ma_T = 5$. Other parameters have the following values: $\zeta = -1$, $Ma_\Gamma = 5$, $Pe_s = 0.1$, $\delta = 0.1$, $\lambda = 0.1$, $e = 0$ and $R = 5$.

eccentrically located droplet. An eccentrically located droplet encounters a larger velocity at the north pole (as it is closer to channel centreline) and smaller velocity at the south pole (as it is away from the channel centreline), as depicted in figure 1. Asymmetry in $\Gamma(\theta, \varphi)$ creates asymmetry in $\sigma(\theta, \varphi)$ (refer to figure 8*b*), which leads to the generation of hydrodynamic forces in both the axial and transverse directions which cause the cross-stream migration of the eccentrically located droplet. The distributions of $\Gamma(\theta, \varphi)$ and $\sigma(\theta, \varphi)$ in non-isothermal Poiseuille flow (i.e. $Ma_T > 0$) for $\zeta = 1$ (i.e. increasing temperature in the direction of Poiseuille flow) and $e = 1$ are shown in figures 8(*c*) and 8(*d*), respectively. For $\zeta = 1$ the thermocapillary-induced Marangoni flow drives surfactants from the east pole to the west pole and increases the asymmetry in $\Gamma(\theta, \varphi)$, which leads to maximum surfactant concentration near the northwest pole and minimum surfactant concentration near the northeast pole. Comparison of figures 8(*c*) with 8(*a*) reflects the increase in asymmetry in terms of an increase in $(\Gamma_{max} - \Gamma_{min})$. This surfactant distribution combined with the non-uniform temperature distribution leads to larger $\sigma(\theta, \varphi)$ near the west pole as compared with the east pole (refer to figure 8*d*). Similar to $\Gamma(\theta, \varphi)$, an increase in asymmetry about the axial plane is also present in $\sigma(\theta, \varphi)$ (i.e. $(\sigma_{max} - \sigma_{min})$), which further leads to an increase in magnitude of the cross-stream velocity of the droplet.

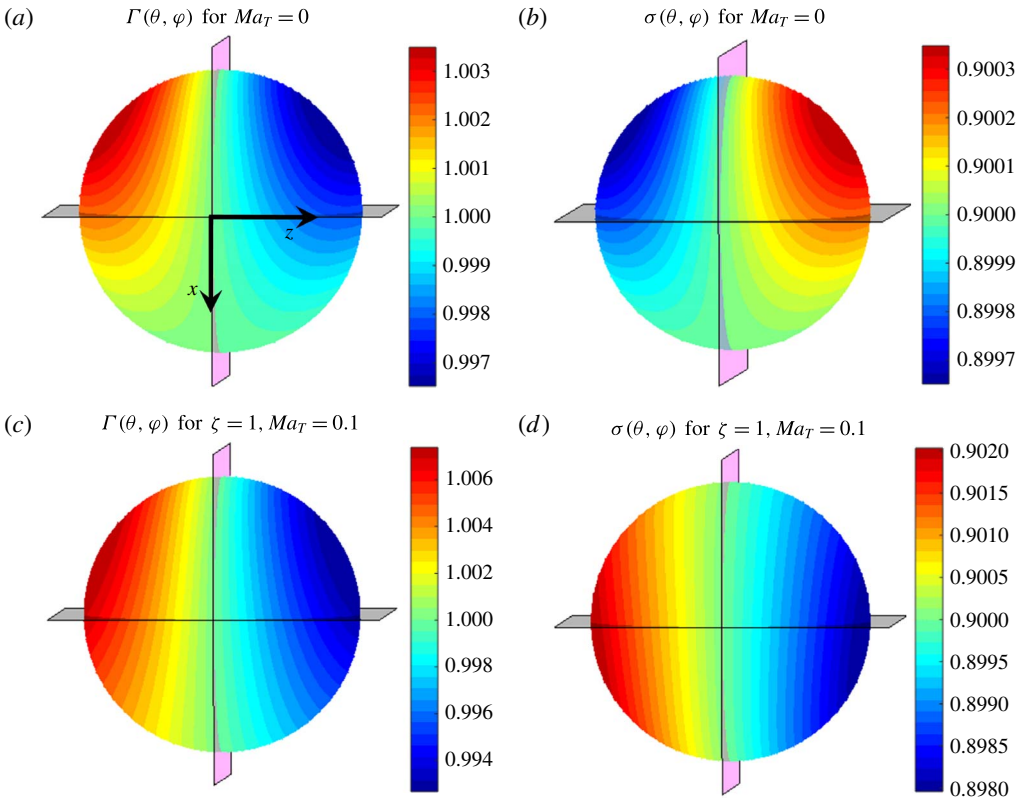


FIGURE 8. (Colour online) Surface plot showing the variation of the surfactant concentration for (*a*) $Ma_T = 0$, (*c*) $\zeta = 1$ and $Ma_T = 0.1$. Surface plot showing the variation of the interfacial tension for (*b*) $Ma_T = 0$, (*d*) $\zeta = 1$ and $Ma_T = 0.1$. The other parameters are $Ma_\Gamma = 5$, $Pe_s = 0.1$, $\delta = 0.1$, $\lambda = 0.1$, $e = 1$ and $R = 5$.

The distributions of $\Gamma(\theta, \varphi)$ in non-isothermal Poiseuille flow (i.e. $Ma_T > 0$) for $\zeta = -1$ (i.e. decreasing temperature in the direction of Poiseuille flow) and $e = 1$ are shown in figure 9. For $\zeta = -1$ the thermocapillary-induced Marangoni flow drives surfactants from the west to the east pole, while the imposed Poiseuille flow drives the surfactant in the opposite direction (i.e. from the east to the west pole). The final surfactant distribution is decided by the net surface velocity. For $Ma_T < Ma^*_{T,x}$, the Poiseuille flow dominates over the thermocapillary-induced Marangoni flow and leads to a maximum surfactant concentration near the northwest pole and a minimum surfactant concentration near the northeast pole (refer to figure 9*a*). This distribution is similar to the case of $\zeta = 1$ (refer to figure 8*c*), which leads to cross-stream motion of droplets towards the channel centreline. However, when thermocapillary-induced Marangoni stress dominates over the Poiseuille flow (for $Ma_T > Ma^*_{T,x}$), the surfactant concentration is maximum near the southeast pole and minimum near the southwest pole (refer to figure 9*b*). This is completely opposite to that of $Ma_T < Ma^*_{T,x}$ (shown in figure 9*a*). This asymmetric distribution of $\Gamma(\theta, \varphi)$ leads to cross-stream migration of the droplet away from the channel centreline.

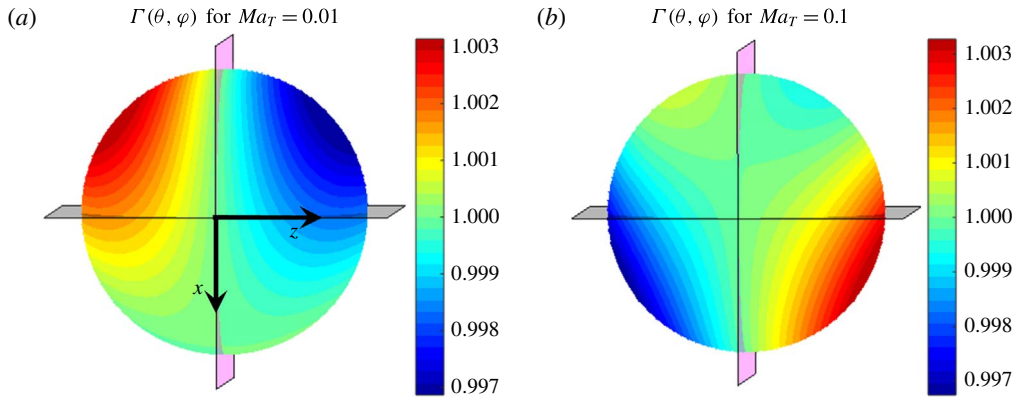


FIGURE 9. (Colour online) Surface plot showing the variation of the surfactant concentration for (*a*) $Ma_T = 0.01$ and (*b*) $Ma_T = 0.1$. Other parameters have the following values: $\zeta = -1$, $Ma_\Gamma = 5$, $Pe_s = 0.1$, $\delta = 0.1$, $\lambda = 0.1$, $e = 1$ and $R = 5$.

4.1.2. *Effect of Marangoni stress in the high-$Pe_s$ limit*

We have obtained the velocity of a neutrally buoyant droplet in the high-$Pe_s$ limit as

$$\boldsymbol{U} = \left[1 - \frac{2}{3R^2} - \left(\frac{e}{R}\right)^2\right] \boldsymbol{e}_z - Ma_\Gamma^{-1} \left[\frac{e(4 + 3Ma_T \zeta R^2 + 2\delta)}{3R^4(\delta + 2)}\right] \boldsymbol{e}_x + O(Ma_\Gamma^{-2}). \tag{4.4}$$

Substituting $Ma_T = 0$ in (4.4), we recover the velocity of a surfactant-laden droplet in isothermal Poiseuille flow in the large-$Pe_s$ limit. However, this result does not match with that obtained by Hanna & Vlahovska (2010). The reason for this mismatch lies in the choice of imposed flow. Hanna & Vlahovska (2010) did their analysis for the case of an imposed plane Poiseuille flow, whereas the present study involves a circular Poiseuille flow. Had the present analysis been repeated for the case of a planar Poiseuille flow, an exact match with the results of Hanna & Vlahovska (2010) would have been inevitable. A closer look into (4.4) reveals that the thermocapillary-induced Marangoni stress only affects the cross-stream velocity of the droplet.

Now, we investigate the effects of Marangoni stresses on the cross-stream velocity of the droplet. Towards this, we first plot figure 10(*a*), which shows the variation of droplet velocity in the cross-stream direction ($U_x$) with the conductivity ratio ($\delta$) for the particular case in which the temperature increases in the direction of the Poiseuille flow (i.e. $\zeta = 1$). Figure 10(*a*) depicts that in the presence of temperature variation (i.e. $Ma_T > 0$), there is a significant increase in the magnitude of the cross-stream velocity (i.e. $|U_x|$). So the thermocapillary-induced Marangoni stress aids the surfactant-induced cross-stream migration of the droplet for $\zeta = 1$. The magnitude of the cross-stream velocity increases with increasing $Ma_T$ for low-conductivity droplets. With an increase in the thermal conductivity of the droplet, the cross-stream velocity reduces. An interesting thing happens for $\zeta = -1$ (i.e. decreasing temperature in the direction of Poiseuille flow), which is depicted in figure 10(*b*). Similar to the low-$Pe_s$ limit, the thermocapillary-induced Marangoni stress not only alters the magnitude but also the direction of cross-stream migration for $\zeta = -1$. For smaller values of $Ma_T$ (e.g. $Ma_T = 0.01$) the droplet moves towards the channel centreline (i.e. $U_x < 0$). However, for larger values of $Ma_T$ (e.g. $Ma_T = 1$) the droplet moves

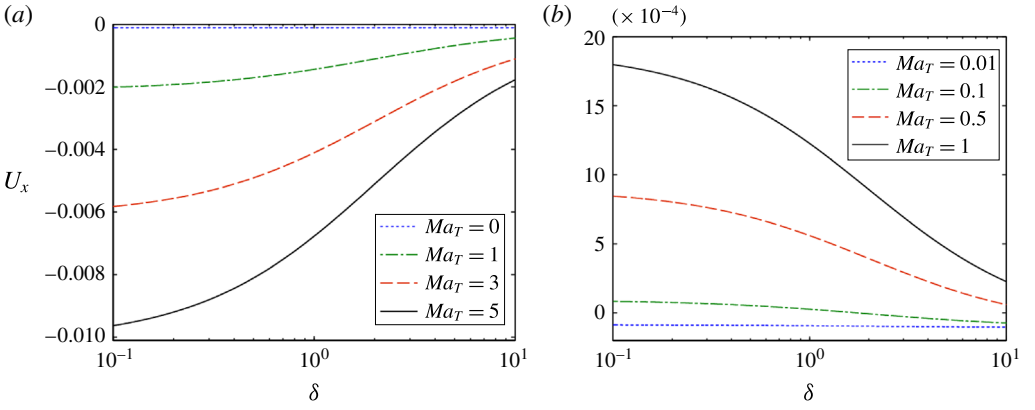


FIGURE 10. (Colour online) Variation of the cross-stream velocity ($U_x$) with the conductivity ratio ($\delta$) for (*a*) $\zeta = 1$ and (*b*) $\zeta = -1$. Other parameters values are $Ma_\Gamma = 10$, $e = 1$ and $R = 5$.

away from the channel centreline (i.e. $U_x > 0$). One can find a critical value of $Ma_T$ for which $U_x = 0$ in the following form:

$$Ma^*_{T,x} = \frac{2}{3R^2}(\delta + 2). \tag{4.5}$$

It is important to note that for $Ma_T < Ma^*_{T,x}$ the magnitude of cross-stream velocity decreases with increasing $Ma_T$, while the magnitude of cross-stream velocity increases with increasing $Ma_T$ for $Ma_T > Ma^*_{T,x}$. Another important thing to note from figure 10 is that the magnitude of the cross-stream velocity for the high-$Pe_s$ limit is much larger compared with the magnitude of the cross-stream velocity for the low-$Pe_s$ limit (refer to figures 4 and 5).

Similar to the low-$Pe_s$ limit, to investigate the alteration in magnitude and direction of the droplet velocity in the axial and cross-stream directions, we plot the distribution of $\Gamma(\theta, \varphi)$ on the surface of an eccentrically located droplet for isothermal Poiseuille flow (with $Ma_T = 0$) in figure 11(*a*) and for non-isothermal Poiseuille flow (with $Ma_T = 0.5$ and $\zeta = 1$) in figure 11(*b*). Figure 11(*a*) depicts that $\Gamma(\theta, \varphi)$ is asymmetric about both the axial and transverse planes, which results in alteration in both the axial and cross-stream velocities. It is important to note that the extent of asymmetry, which can be represented by $(\Gamma_{max} - \Gamma_{min})$, is much larger for the high-$Pe_s$ limit solution as compared with the low-$Pe_s$ limit solution. This is the reason for the larger magnitude in cross-stream velocity of the droplet for the high-$Pe_s$ limit. In the presence of a non-uniform temperature distribution, this asymmetry increases (refer to figure 11*b*), which leads to greater droplet velocities.

The effect of decreasing temperature in the direction of Poiseuille flow (i.e. $\zeta = -1$) is shown in figure 11(*c*) for $Ma_T = 0.01$ and in figure 11(*d*) for $Ma_T = 0.5$. For $Ma_T = 0.01$, $\Gamma(\theta, \varphi)$ is maximum near the northwest pole and minimum near the northeast pole, which is very similar to the case of $Ma_T = 0$. This kind of distribution of $\Gamma(\theta, \varphi)$ leads to motion of the droplet towards the channel centreline. However, for $Ma_T = 0.5$ we obtain that $\Gamma(\theta, \varphi)$ is maximum near the southeast pole and minimum near the southwest pole, which results in cross-stream motion of the droplet away from the channel centreline.

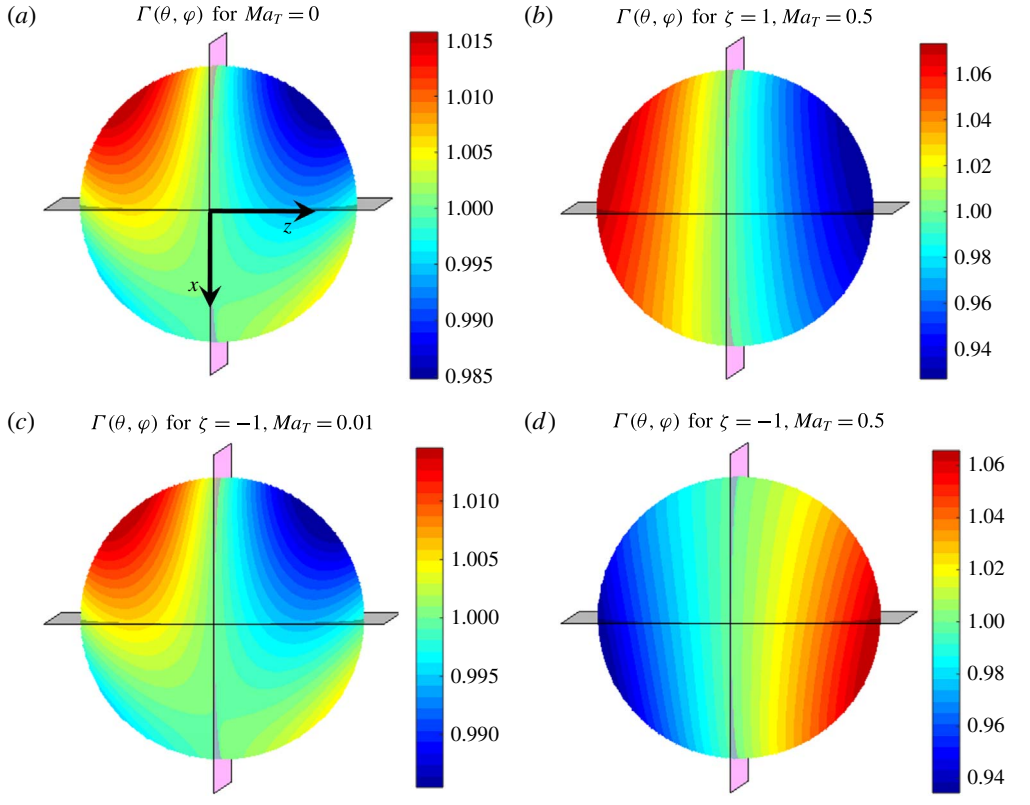


FIGURE 11. (Colour online) Surface plot showing the surfactant distribution for (*a*) $Ma_T = 0$, (*b*) $\zeta = 1$ and $Ma_T = 0.5$, (*c*) $\zeta = -1$ and $Ma_T = 0.01$, (*d*) $\zeta = -1$ and $Ma_T = 0.5$. Other parameters have the following values: $Ma_\Gamma = 10$, $\lambda = 0.1$, $\delta = 0.1$, $e = 1$ and $R = 5$.

### 4.2. *Buoyant droplet* ($Bo \neq 0$)

#### 4.2.1. *Effect of buoyancy in an isothermal flow* ($Ma_T = 0$)

We first consider the case of a surfactant-laden buoyant droplet suspended in an isothermal pressure-driven flow in the limiting case of low surface Péclet number. The droplet velocity in such a scenario is given by

$$\begin{aligned}\boldsymbol{U} = & \left[\begin{array}{l} \dfrac{2}{3}\left(\dfrac{\xi Bo}{Ca}\right)\left(\dfrac{1+\lambda}{3\lambda+2}\right) + \left\{1 - \left(\dfrac{e}{R}\right)^2 - \left(\dfrac{5\lambda}{3\lambda+2}\right)\dfrac{2}{5R^2}\right\} \\ -\dfrac{Ma_\Gamma}{(3\lambda+2)^2}\left[\dfrac{2\xi}{9}\dfrac{Bo}{Ca} + \dfrac{2}{3R^2}\right] Pe_s + \dfrac{2Ma_\Gamma^2}{3(3\lambda+2)^3}\left[\dfrac{\xi Bo}{3Ca} + \dfrac{2}{R^2}\right] Pe_s^2 \end{array}\right] \boldsymbol{e}_z \\ & - \left[\dfrac{Ma_\Gamma e}{5(3\lambda+2)^2(\lambda+1)R^2}\left[(5\lambda+3)\dfrac{\xi Bo}{9Ca} + \dfrac{70\lambda^2+109\lambda+40}{21(\lambda+1)}\right] Pe_s^2\right] \boldsymbol{e}_x \\ & + O(Pe_s^3). \end{aligned} \tag{4.6}$$

Towards discussing the effect of buoyancy force on the cross-stream migration velocity of the surfactant-laden droplet in the low-$Pe_s$ limit, we first plot the variation of the cross-stream migration velocity with $\lambda$ for different values of $Bo/Ca$ for the special cases of $\xi = 1$ and $\xi = -1$. We first analyse the former case where $\rho_i > \rho_e$, that is the

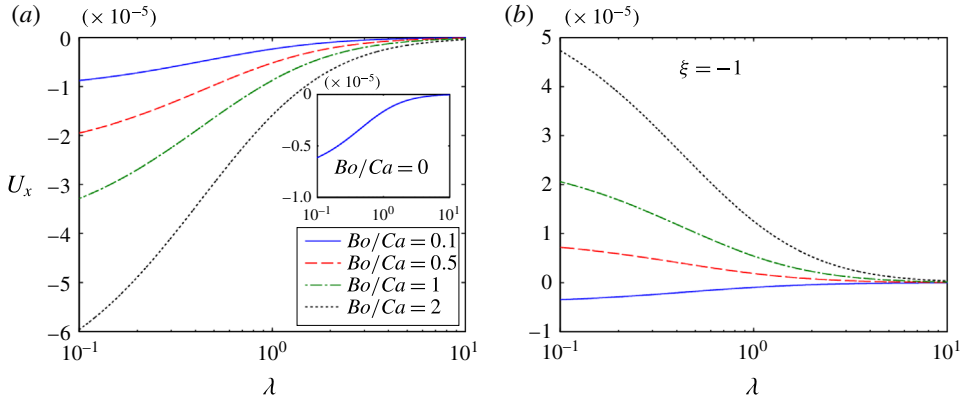


FIGURE 12. (Colour online) Variation of the cross-stream migration velocity with $\lambda$ for different values of $Bo/Ca$ (0.1, 0.5, 1, 2) in an isothermal flow field ($Ma_T = 0$). In (*a*) the buoyancy force acts in the direction of imposed flow ($\xi = 1$), while in (*b*) the buoyancy force acts opposite to the direction of imposed flow ($\xi = -1$). Other parameters have the following values: $Ma_\Gamma = 5$, $Pe_s = 0.1$, $\delta = 0.1$, $e = 1$ and $R = 5$.

buoyancy force acts in the same direction as the imposed Poiseuille flow. It is seen from figure 12(*a*) that an increase in the buoyancy force, and hence a rise in $Bo/Ca$, results in an increase in the cross-stream migration velocity. This effect of buoyancy force on the cross-stream migration of the droplet is seen to be higher for the case of a low-viscosity droplet. The inset in figure 12(*a*) shows the variation of cross-stream droplet velocity for the case of a neutrally buoyant droplet ($Bo/Ca = 0$). The same result was reported by Pak *et al.* (2014). On comparison with the inset, it is seen that the presence of a buoyancy force in the axial direction increases the cross-stream migration velocity significantly.

A physical explanation for the variation of the cross-stream migration velocity of the droplet with buoyancy force can be provided if we look closely at the surface plot displaying the surfactant distribution along the droplet surface, as shown in figure 13. Since asymmetry in the surfactant concentration across the axial plane is the source for cross-stream migration of the droplet, we first study the effect of buoyancy force on the variation of the surfactant distribution. It is to be noted that the fluid flow along the surface of an eccentrically placed droplet is affected equally due to the presence of buoyancy force, unlike the case of an imposed Poiseuille flow explained before. However, the buoyancy force enhances the asymmetry in the surfactant distribution already induced by the imposed pressure-driven flow on the eccentrically located droplet. This is because the presence of the buoyancy force in the direction of the imposed flow increases the net hydrodynamic force acting on the droplet and increases the fluid flow velocity along the droplet surface. As can be seen on comparison between figures 8(*a*) and 13, the presence of the buoyancy force in the axial direction increases the gradient in the surfactant concentration, $|\Gamma_{max} - \Gamma_{min}|$, with the highest surfactant concentration in the northwestern region and the minimum in the northeastern region. This results in an increase in the Marangoni stress which drives the droplet towards the centreline with a higher migration velocity.

We next consider the special case where the buoyancy force acts in a direction opposite to the imposed flow, that is $\rho_i < \rho_e$ or $\xi = -1$. Figure 12(*b*) shows the variation of the cross-stream migration velocity with $\lambda$, for different values of $Bo/Ca$. Similar to figure 5, any increase in the buoyancy force (or $Bo/Ca$) initially results in

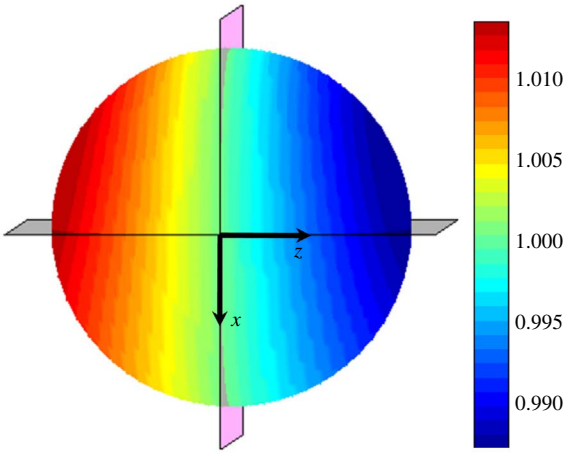


FIGURE 13. (Colour online) Surface plot showing the surfactant distribution over the surface of the droplet suspended in an isothermal flow ($Ma_T = 0$). The buoyancy force increases in the direction of the imposed flow ($\xi = 1$). Other important parameters involved are $Pe_s = 0.1$, $Ma_\Gamma = 5$, $Ma_T = 0$, $\delta = 0.1$, $R = 5$, $e = 1$, $Bo/Ca = 1$ and $\lambda = 0.1$.

a decrease in the cross-stream migration velocity. This goes on until a critical point is reached corresponding to which there is no cross-stream migration of the droplet. The critical value of $Bo/Ca$ is obtained from (4.6) as

$$\left(\frac{Bo}{Ca}\right)^*_x = \frac{3}{7}\left\{\frac{70\lambda^2 + 109\lambda + 40}{(\lambda+1)(5\lambda+3)}\right\}, \tag{4.7}$$

which signifies the critical buoyancy force acting on the droplet. From figure 12(*b*) it can be seen that the droplet migrates towards the centreline for a low value of $Bo/Ca$ (lower than its critical value). The magnitude of the cross-stream migration velocity of the droplet reduces with an increase in the value of $Bo/Ca$ until its critical value $(Bo/Ca)^*$ is reached. Beyond the critical value, the droplet migrates away from the centreline and its cross-stream velocity keeps on increasing with an increase in the buoyancy force.

Again, a proper physical explanation can be provided if we look into the surface plots showing the surfactant distribution along the droplet surface. In the present situation, the buoyancy force and the hydrodynamic force due to the imposed Poiseuille flow oppose each other. Depending on which of the two dominates, the droplet may migrate towards the centreline of flow or away from it. Initially, for the case of low buoyancy force, the Poiseuille flow dominates. However, the net hydrodynamic force reduces with an increase in the buoyancy force, which in turn decreases the flow at the interface. This results in reduced asymmetry in the surfactant distribution across the axial plane of the droplet, and hence a lower Marangoni stress responsible for the cross-stream migration of the droplet. This explains the decrease in the cross-stream migration velocity of the droplet. Figure 14(*a*) shows the surfactant distribution along the droplet surface for the special case when $Bo/Ca < (Bo/Ca)^*$. This distribution has a similar resemblance to that obtained in figure 8(*a*) in the absence of any buoyancy force. This confirms that the droplet migrates towards the centreline; however, the magnitude of $|\Gamma_{max} - \Gamma_{min}|$ is lower for the present case, which proves that the Marangoni stress is lower and hence the associated decrease

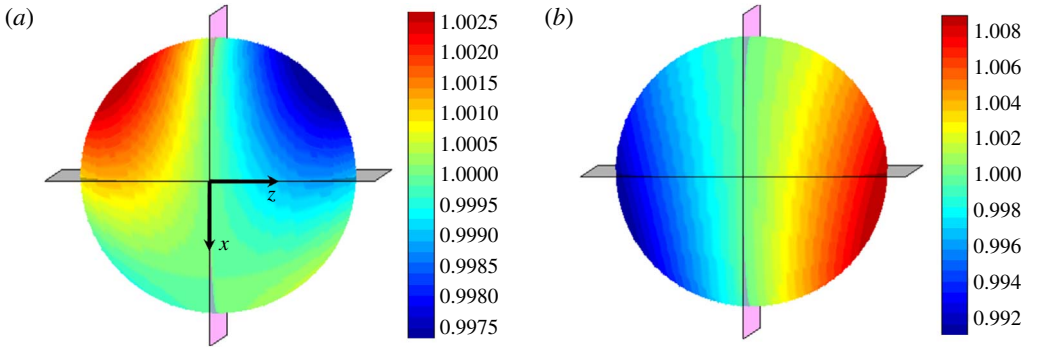


FIGURE 14. (Colour online) Surface plot showing the surfactant distribution over the surface of the droplet suspended in an isothermal flow ($Ma_T = 0$). The buoyancy force increases opposite to the direction of the imposed flow ($\xi = -1$). (*a*) is plotted for $Bo/Ca = 0.1$, while (*b*) is plotted for $Bo/Ca = 1$. Other important parameters involved are $Pe_s = 0.1$, $Ma_\Gamma = 5$, $Ma_\Gamma = 0$, $\delta = 0.1$, $R = 5$, $e = 1$ and $\lambda = 0.1$.

in cross-stream migration velocity. For the other case of $Bo/Ca > (Bo/Ca)^*$, the buoyancy force dominates, and hence the fluid flow direction on the droplet surface changes, which alters the surfactant distribution altogether, as can be seen from figure 14(*b*). The surfactant is seen to have a higher concentration in the southeast region of the droplet surface while the lowest concentration is in the southwest region of the droplet. This distribution of surfactants results in lateral migration of the droplet away from the centreline of flow. On comparison of figures 8(*a*) and 14(*b*), it can be said that the presence of the buoyancy force increases the magnitude of $|\Gamma_{max} - \Gamma_{min}|$ (surfactant gradient along the surface) provided that $(Bo/Ca) > (Bo/Ca)^*$, which further increases the cross-stream migration velocity of the droplet.

Now, we consider the high-$Pe_s$ limit. This limiting case considers surface-convection-dominated surfactant transport along the droplet surface. The droplet migration velocity in this limit is given by

$$\boldsymbol{U} = \left[\left\{\frac{2\xi Bo}{9Ca} + 1 - \frac{2}{3R^2} - \left(\frac{e}{R}\right)^2\right\}\boldsymbol{e}_z - Ma_\Gamma^{-1}\frac{e}{R^2}\left\{\frac{\xi Bo}{9Ca} + \frac{2}{3R^2}\right\}\boldsymbol{e}_x\right] + O(Ma_\Gamma^{-2}). \quad (4.8)$$

As can be seen from the above expression, both the axial as well as the cross-stream migration velocities of the droplet under this limit are independent of the viscosity ratio. The axial velocity is directly proportional to the buoyancy force and any increase in $Bo/Ca$ results in an increase of the same. For the case of $\xi = 1$, the droplet migrates in the direction of the imposed flow. Similar to the low-$Pe_s$ limit, the direction of axial migration changes depending on the magnitude of $Bo/Ca$ for the special case of $\xi = -1$. The critical value of $Bo/Ca$ for this limit is given by

$$\left(\frac{Bo}{Ca}\right)_z^* = \frac{9}{2}\left\{1 - \frac{2}{3R^2} - \left(\frac{e}{R}\right)^2\right\}. \quad (4.9)$$

The expression for the cross-stream migration, as seen from (4.8), is dependent solely on the buoyancy force. For the case of $\xi = 1$, the increase in buoyancy force increases the cross-stream migration velocity of the droplet while it migrates towards the centreline of flow. For the other case, $\xi = -1$, depending on the value of $Bo/Ca$

the droplet may migrate towards or away from the centreline. The corresponding critical value of $Bo/Ca$ is given by

$$\left(\frac{Bo}{Ca}\right)^{*}_{x} = \frac{6}{R^2}. \tag{4.10}$$

4.2.2. *Effect of buoyancy force in non-isothermal flow* ($Ma_T \neq 0$)*: low-*$Pe_s$ *limit*

The velocity of a buoyant droplet (gravity acting in the direction of Poiseuille flow) for the low-$Pe_s$ limit under the combined presence of imposed Poiseuille flow and a linearly varying temperature field is given by

$$\begin{aligned}\boldsymbol{U} = & \left[\begin{array}{l} \dfrac{2}{3}\left(\dfrac{\xi Bo}{Ca}\right)\left(\dfrac{1+\lambda}{3\lambda+2}\right)+\left\{1-\left(\dfrac{e}{R}\right)^2-\left(\dfrac{5\lambda}{3\lambda+2}\right)\dfrac{2}{5R^2}\right\}+\dfrac{2\zeta Ma_T}{(3\lambda+2)\,(\delta+2)} \\ \quad -\dfrac{Ma_\Gamma}{(3\lambda+2)^2}\left[\dfrac{2\xi}{9}\dfrac{Bo}{Ca}+\left\{\dfrac{Ma_T\zeta}{(\delta+2)}+\dfrac{2}{3R^2}\right\}\right]Pe_s \\ \quad +\dfrac{2Ma_\Gamma^2}{3(3\lambda+2)^3}\left[\dfrac{\xi Bo}{3Ca}+\dfrac{2}{R^2}+\dfrac{3Ma_T\zeta}{(2+\delta)}\right]Pe_s^2 \end{array}\right]\boldsymbol{e}_z \\ & + \left[-\frac{Ma_\Gamma e}{5(3\lambda+2)^2(\lambda+1)R^2}\left[(5\lambda+3)\left\{\frac{\xi Bo}{9Ca}+\frac{Ma_T\zeta}{(2+\delta)}\right\}\right.\right. \\ & \left.\left.+\frac{70\lambda^2+109\lambda+40}{21(\lambda+1)}\right]Pe_s^2\right]\boldsymbol{e}_x+O(Pe_s^3). \end{aligned} \tag{4.11}$$

In contrast to the neutrally buoyant droplet, an interesting point to note from (4.11) is that the cross-stream migration velocity is dependent on the buoyancy force even though gravity acts in the axial direction. In the absence of any imposed flow, the migration velocity for a clean buoyant droplet in a linearly varying temperature field is simply given by substituting $Ma_\Gamma = 0$ in (4.11). The resulting expression for the droplet velocity in its dimensional form is given by

$$\bar{\boldsymbol{U}}_{YGB} = \left[-\frac{2}{3}\frac{(\lambda+1)(\rho_e-\rho_i)ga^2}{\mu_e(3\lambda+2)}+\frac{2\beta|G|a}{\mu_e(\delta+2)(3\lambda+2)}\right]\boldsymbol{e}_z, \tag{4.12}$$

which is the same as that obtained by Young *et al.* (1959).

We now analyse the effect of thermal Marangoni stress on droplet migration in the presence of a buoyancy force. As our primary objective is the analysis of the cross-stream migration velocity of the droplet, we do not show any variation of the axial migration velocity. Since the buoyancy force is independent of the thermal Marangoni stress, the droplet migration velocity is additive for the following two cases: (1) migration of a neutrally buoyant surfactant-laden droplet in a non-isothermal Poiseuille flow and (2) migration of a surfactant-laden buoyant droplet in an isothermal Poiseuille flow. Both of these cases have been discussed in detail. So in this section we investigate the contribution of both the buoyancy force as well as the thermal Marangoni stress on the cross-stream migration of the droplet. Towards this, we analyse four possible cases, namely (i) $\xi = 1$, $\zeta = 1$: this signifies the case where both the buoyancy force as well as thermally induced Marangoni stresses act in the direction of the imposed flow. That is, we have a denser droplet phase and the applied temperature field linearly increases in the direction of the bulk fluid flow. (ii) $\xi = 1$, $\zeta = -1$: this indicates the situation where the buoyancy force remains

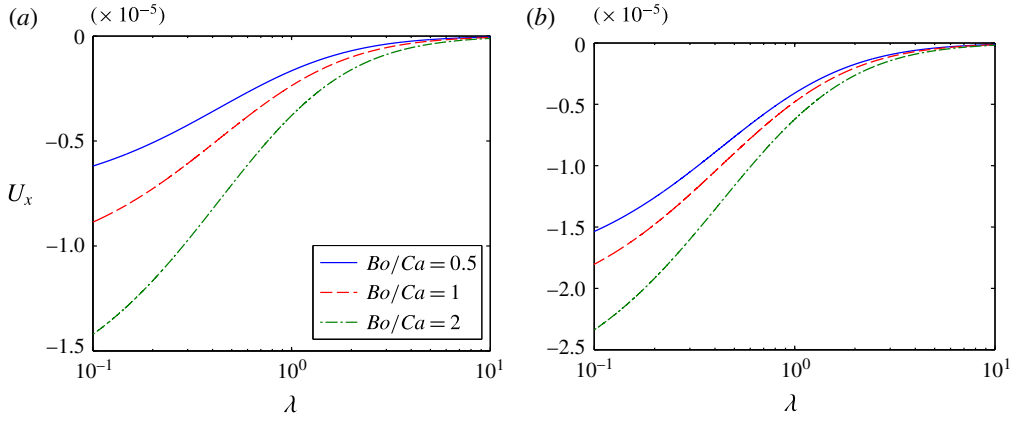


FIGURE 15. (Colour online) Variation of the cross-stream migration velocity with $\lambda$ for different values of $Bo/Ca$ (0.5, 1, 2) when the applied temperature gradient is along the positive $z$-direction. In ($a$) we have $Ma_T = 0.1$, while in ($b$) the applied temperature gradient is increased such that $Ma_T = 0.5$. Other parameters have the following values: $Ma_\Gamma = 1$, $Pe_s = 0.1$, $\delta = 0.1$, $e = 1$ and $R = 5$.

unchanged while the applied temperature field decreases linearly in the direction of the imposed flow. (iii) $\xi = -1$, $\zeta = 1$: compared to the first case, this involves a denser carrier phase, and hence the buoyancy force acts opposite to the direction of the imposed flow. The applied temperature field is kept the same. (iv) $\xi = -1$, $\zeta = -1$: this is the situation which is completely opposite to that of the first case.

We first look into case (i). The variation of the cross-stream migration velocity with $\lambda$ for different values of $Bo/Ca$ is shown in figure 15($a$). The same plot is repeated for a higher value of $Ma_T(= 0.5)$ to show the effect of the thermal Marangoni stress. For the present case, it can be seen from figure 15($a$,$b$) that as $Bo/Ca$ increases, the magnitude of the cross-stream migration velocity of the droplet also increases. The parameter $Bo/Ca$ can be varied between 0.1 and 2 by choosing different varieties of silicone oil, resulting in different density differences, and hence different values of $Bo$. On comparison of figures 15($a$) and 4, it can be seen that presence of buoyancy force in the system increases the cross-stream velocity of the droplet. This is because the buoyancy force acts in the direction of the applied temperature gradient and hence induces a hydrodynamic flow with an additive effect to the thermal Marangoni stress, which propels the droplet towards the centreline of flow. Comparison of figures 15($a$) and 15($b$) indicates that an increase in $Ma_T$ in the presence of the buoyancy effect further enhances the cross-stream migration velocity of the droplet.

We next investigate the case (ii) where we have a negative temperature gradient ($\zeta = -1$). It can be seen from figure 16 that buoyancy, although acting in the axial direction, plays a significant role in altering the magnitude as well as the direction of the cross-stream migration velocity. Similar to the case of the neutrally buoyant droplet, a critical thermal Marangoni number can be defined for the present scenario which depends on $Bo$ and is given by

$$Ma^*_{T,x} = (\delta + 2)\left\{\frac{Bo}{9Ca} + \frac{(70\lambda^2 + 109\lambda + 40)}{21(5\lambda + 3)(\lambda + 1)R^2}\right\}. \tag{4.13}$$

From the above equation it is obvious that an increase in $Bo$ results in an increase in the critical Marangoni number. In figure 16 we consider a constant value for

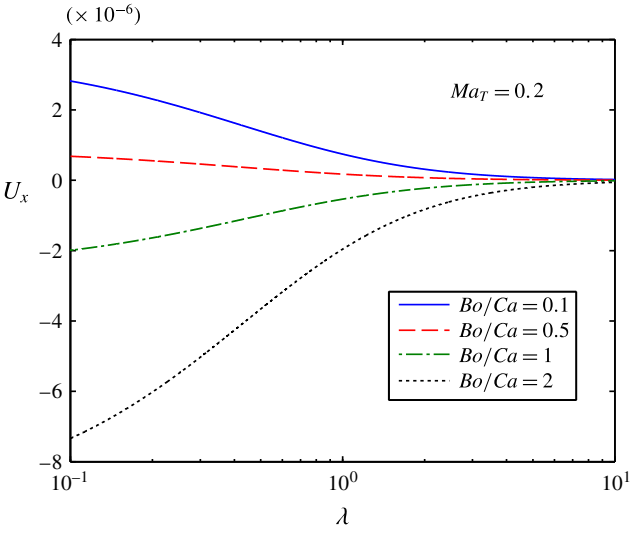


FIGURE 16. (Colour online) Variation of the cross-stream migration velocity with $\lambda$ for different values of $Bo/Ca$ (0.1, 0.5, 1, 2) when $\xi = 1$, $\zeta = -1$. Other parameters have the following values: $Ma_\Gamma = 1$, $Ma_T = 0.2$, $Pe_s = 0.1$, $\delta = 0.1$, $e = 1$ and $R = 5$.

the applied temperature gradient (e.g. $Ma_T = 0.2$) and gradually increase $Bo/Ca$ by choosing different varieties of silicone oil resulting in larger density differences. Initially for a low value of $Bo/Ca$, the thermal Marangoni stress dominates over the combined effect of imposed flow and the buoyancy force, which forces the droplet to migrate away from the centreline of flow. With an increase in the buoyancy force on the droplet relative to the pressure and viscous forces ($Bo/Ca$) and a corresponding rise in $Ma^*_{T,x}$, the magnitude of the cross-stream migration of the droplet gradually reduces until the relation $Ma_T > Ma^*_{T,x}$ holds. Finally, when $Ma_T = Ma^*_{T,x}$, the cross-stream motion of the droplet stops. A further increase in the buoyancy force beyond this critical point results in $Ma_T < Ma^*_{T,x}$. This indicates the fact that the buoyancy force along with the hydrodynamic force overcome the effect of the thermal Marangoni stress. Any further increase in $Bo/Ca$ increases the net force acting on the droplet, and hence the asymmetry in the surfactant distribution. Thus, the cross-stream migration velocity of the droplet goes on increasing, which now migrates towards the flow centreline. It can be seen from both figures 15 and 16 that buoyancy does not have a sufficient effect on the cross-stream velocity for a highly viscous droplet ($\lambda > 10$). This is due to the fact that at high values of $\lambda$, the droplet behaves as a particle, which renders any non-uniform distribution of surfactants ineffective on variation of the surface tension. Hence the coupling that existed between the buoyancy and Marangoni stress breaks, resulting in no cross-stream motion of the droplet, irrespective of the magnitude of the buoyancy force. Thus, buoyancy at this regime of high $\lambda$ only results in a higher axial migration velocity.

We next analyse the special case (iii) where $\xi = -1$ and $\zeta = 1$. For this particular scenario, the buoyancy force opposes the hydrodynamic force due to the combined effect of the temperature gradient and the imposed flow. The critical thermal Marangoni number is thus given by

$$Ma^*_{T,x} = (2 + \delta)\left\{\frac{Bo}{9Ca} - \frac{70\lambda^2 + 109\lambda + 40}{21(\lambda + 1)(5\lambda + 3)}\right\}. \tag{4.14}$$

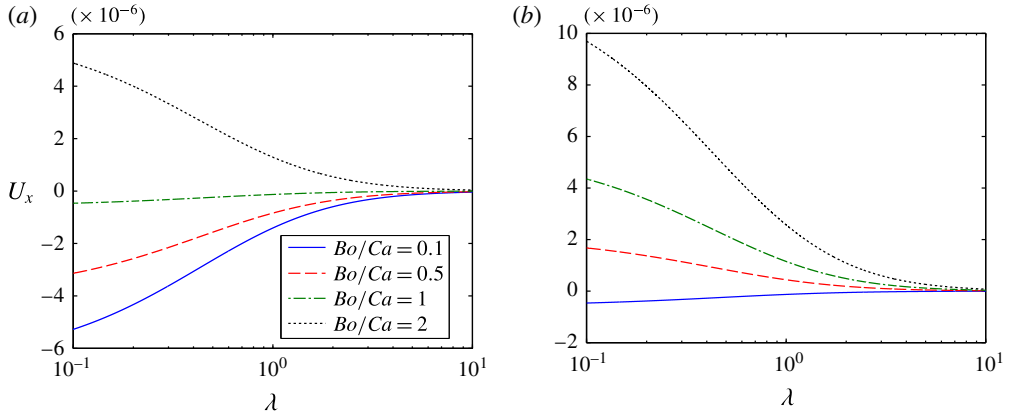


FIGURE 17. (Colour online) Variation of cross-stream migration velocity with $\lambda$ for different values of $Bo/Ca$ (0.1, 0.5, 1, 2) when the buoyancy force acts along the negative $z$-direction ($\xi = -1$). In (*a*) $Ma_T = 0.2$, $\zeta = 1$, while in (*b*) $Ma_T = 0.01$, $\zeta = -1$. Other parameters have the following values: $Ma_\Gamma = 1$, $Pe_s = 0.1$, $\delta = 0.1$, $e = 1$ and $R = 5$.

As can be seen from the above expression, a larger buoyancy force results in an increase in the critical Marangoni number. To understand the role of $Ma^*_{T,x}$, we plot the cross-stream migration velocity with $\lambda$ for different values of $Bo/Ca$, which is displayed in figure 17(*a*). It can be seen from the figure that for a low value of $Bo/Ca$, the droplet migrates towards the centreline of flow until $Ma_T > Ma^*_{T,x}$. This is due to the nature of the surfactant distribution, which is similar to figure 8(*c*). On increasing $Bo/Ca$, the value of $Ma^*_{T,x}$ also increases, and at the same time the magnitude of the cross-stream migration velocity reduces due to a decrease in the surfactant concentration gradient $|\Gamma_{max} - \Gamma_{min}|$. On further increasing $Bo/Ca$, the critical point is finally attained where $Ma_T = Ma^*_{T,x}$ and there is no cross-stream migration. Increasing the buoyancy force beyond this point ($Ma_T < Ma^*_{T,x}$) results in an increase in the cross-stream migration velocity of the droplet, which now migrates away from the flow centreline. Such a variation of the cross-stream migration velocity is shown in figure 17(*a*).

We now discuss the final situation where both the buoyancy as well as the thermal Marangoni stress acts in the opposite direction to that of the imposed flow (case (iv)). Thus, depending on whether the hydrodynamic force due to imposed flow dominates over the other effects or not, the fluid flow, and hence the surfactant, redistributes itself along the surface of the droplet. The asymmetry of the surfactant distribution about the axial plane decides the magnitude as well as the direction of migration of the droplet in the cross-stream direction. In figure 17(*b*) we have shown the variation of the cross-stream migration velocity of the droplet with $\lambda$ for different values of $Bo/Ca$. It is seen from the figure that for low values of both $Ma_T$ (= 0.01) and $Bo/Ca$ (= 0.1), the hydrodynamics force due to the imposed flow dominates, and hence the droplet migrates towards the centreline of flow. Increasing $Bo/Ca$ results in a further decrease in the cross-stream migration velocity until $Ma_T < Ma^*_{T,x}$, where the critical Marangoni number for the present case is defined by

$$Ma^*_{T,x} = (2+\delta)\left\{-\frac{Bo}{9Ca} + \frac{70\lambda^2 + 109\lambda + 40}{21(\lambda+1)(5\lambda+3)}\right\}. \tag{4.15}$$

As seen from the above equation, the magnitude of $Ma^*_{T,x}$ decreases with an increase in the buoyancy force. This critical point of no lateral migration decides the direction

of migration of the droplet. For the case when $Ma_T > Ma^*_{T,x}$, the droplet starts migrating away from the centreline of flow and the magnitude of the cross-stream migration velocity increases with increasing $Bo/Ca$. This variation of the cross-stream migration velocity can be seen in figure 17(*b*).

4.2.3. *Effect of buoyancy force in non-isothermal flow* ($Ma_T \neq 0$)*: high-*$Pe_s$ *limit*

In this limiting case of surface-convection-dominated surfactant transport, we have the velocity of a buoyant droplet as

$$\boldsymbol{U} = \left[\left\{\frac{2\xi Bo}{9Ca} + 1 - \frac{2}{3R^2} - \left(\frac{e}{R}\right)^2\right\}\boldsymbol{e}_z + Ma_\Gamma^{-1}\frac{e}{R^2}\left\{-\frac{\xi Bo}{9Ca} - \left(\frac{2}{3R^2} + \frac{Ma_T\zeta}{\delta+2}\right)\right\}\boldsymbol{e}_x\right] + O(Ma_\Gamma^{-2}). \tag{4.16}$$

It can be seen from the above equation that both the axial as well as the cross-stream migration velocity are dependent on the buoyancy force acting on the droplet. The axial velocity, which is independent of any Marangoni stress (surfactant or thermally induced), is seen to increase with a higher droplet phase density relative to the carrier phase. To analyse the variation of the cross-stream migration velocity, we first analyse case (i) and case (ii), as was discussed in the previous section. We thus plot the cross-stream migration velocity against the thermal conductivity ratio of either of the phases for different values of $Bo/Ca$ (figure 18) for $\xi = 1$. Figure 18(*a*) considers the case in which the temperature increases in the direction of the imposed pressure-driven flow ($\zeta = 1$), while figure 18(*b*) shows the variation for the particular case of $\zeta = -1$. For the case of $\zeta = 1$, the droplet migrates towards the centreline of flow. The cross-stream migration velocity increases with an increase in the buoyancy force ($Bo/Ca$). The presence of the buoyancy force enhances the net Marangoni stress propelling the droplet in the transverse direction by increasing the asymmetry in the distribution of the interfacial tension across the axial plane of the droplet. Due to the enhanced surface convection, the magnitude of the migration velocity is seen to be significantly higher in comparison to the case of low Péclet number. The cross-stream migration velocity is seen to be uniformly affected by the buoyancy force over all ranges of $\delta$.

To investigate the situation for $\zeta = -1$, we first evaluate the critical thermal Marangoni number, which is given by

$$Ma^*_{T,x} = \left[\frac{Bo}{9Ca} + \frac{2}{3R^2}\right](\delta + 2). \tag{4.17}$$

It can be seen from the above expression that the buoyancy has a positive effect on the critical Marangoni number. Hence a similar behaviour for variation of the cross-stream migration velocity as that for the limiting case of low $Pe_s$ for case (i) is expected. As seen from figure 18(*b*), the cross-stream velocity of the droplet decreases with an increase in $Bo/Ca$. Increasing $Bo/Ca$ at the same time increases the value of $Ma^*_{T,x}$. Thus, as long as $Ma_T > Ma^*_{T,x}$, the droplet migrates away from the centreline of the flow. However, for $Ma_T < Ma^*_{T,x}$, the droplet starts migrating towards the centreline with a cross-stream velocity that increases with an increase in the buoyancy force ($Bo/Ca$). The nature of variation of the cross-stream migration velocity as compared to that of the limiting case of low $Pe_s$ is the same, with the only difference in the magnitude of the velocity, which seems to be much higher for the high-$Pe_s$ limit.

Considering the case when the buoyancy force acts in the direction opposite to that of the imposed flow ($\xi = -1$), a similar variation of the cross-stream migration

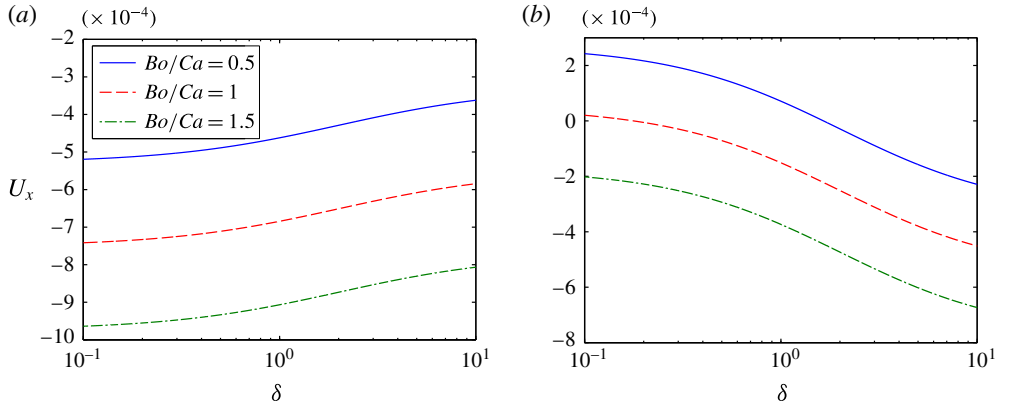


FIGURE 18. (Colour online) Variation of the cross-stream migration velocity with $\delta$ for different values of $Bo/Ca$ (0.5, 1, 1.5) and $\xi = 1$. The plot is shown for two cases: (*a*) the temperature increases in the direction of imposed flow with $Ma_T = 0.1$, (*b*) the applied temperature gradient is in a direction opposite to that of the imposed flow with $Ma_T = 0.3$. Other parameters have the following values: $Ma_\Gamma = 10$, $e = 1$ and $R = 5$.

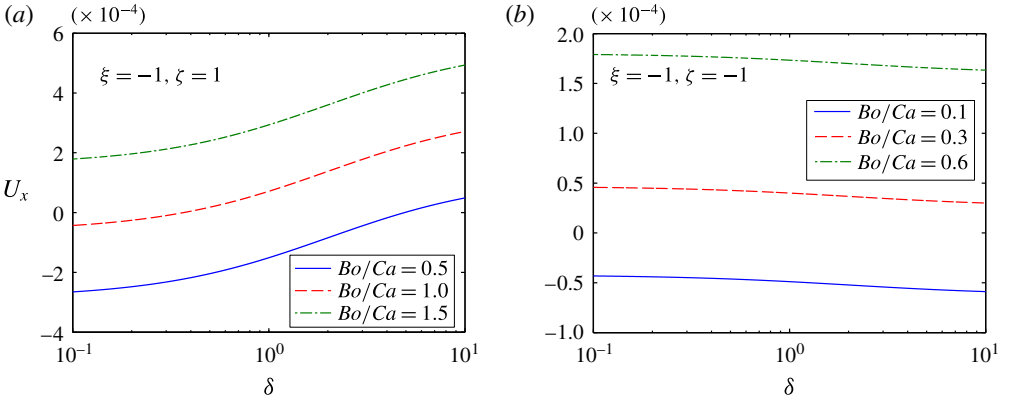


FIGURE 19. (Colour online) Variation of the cross-stream migration velocity with $\delta$ for different values of $Bo/Ca$ and $\xi = -1$ for two different cases: (*a*) the temperature increases in the direction of imposed flow with $Ma_T = 0.2$, (*b*) the applied temperature gradient is in a direction opposite to that of the imposed flow with $Ma_T = 0.01$. Other parameters have the following values: $Ma_\Gamma = 10$, $e = 1$ and $R = 5$.

velocity as in the low-$Pe_s$ limit is seen. Figure 19(*a*,*b*) show the variation of $U_x$ with respect to $\delta$ for different values of $Bo/Ca$. The general expression for $Ma^*_{T,x}$ is given by

$$Ma^*_{T,x} = -\frac{(\delta + 2)}{\zeta}\left(\frac{\xi Bo}{9Ca} + \frac{2}{3R^2}\right). \tag{4.18}$$

With respect to the above expression of $Ma^*_{T,x}$, the direction as well as change in the magnitude of the cross-stream migration velocity of the droplet for both the cases ($\zeta = 1$, $\zeta = -1$) follow a similar trend as in the case of low-$Pe_s$ limit. The magnitude of the migration velocity, however, is higher for the present case due to convection-driven surfactant transport that causes a higher non-uniformity in the surfactant distribution.

## 5. Remarks

The combined effect of temperature and surfactant cannot be obtained by a simple superposition of two existing results (which consider the effects of temperature and surfactant separately). We have derived mathematical relations and shown that the profound effect of temperature field on the cross-stream velocity of the droplet cannot be obtained by simple superposition. The main reason why the linear combination does not work is the nonlinear couplings between the flow field (generated due to imposed Poiseuille flow and thermocapillary-induced Marangoni stress) and the surfactant transport. As per our assumption, the temperature field does not affect the surfactant distribution. This one-way coupling between temperature field and surfactant concentration gives rise to the dominating effect of the temperature field on the cross-stream velocity of the droplet. A simple change in the direction of the applied temperature field results in a change of direction of lateral migration of the droplet. Considering the case of a droplet with a higher density in comparison to the suspending fluid, the droplet always migrates towards the flow centreline if a temperature gradient is applied in the direction of the imposed flow. However, considering the case when the droplet phase is less dense in comparison to the carrier phase, the former may migrate away from the centreline of flow even though a temperature gradient is applied in the direction of the imposed flow. For a sufficiently low density difference between either phases, the droplet moves either towards or away from the flow centreline, depending on the direction of temperature gradient.

## 6. Conclusions

In the present paper, we have analysed droplet motion in an unbounded Poiseuille flow under the combined influence of thermocapillary-induced and surfactant-induced Marangoni stresses. However, it has to be noted that this does not mean a linear superposition of the two effects (that is surfactant-induced and thermocapillary-induced), as the temperature gradient, although applied axially, is found to have a significant effect on the cross-stream migration of the drop. In the absence of fluid inertia, thermal convection and shape deformation, we have obtained asymptotic solutions for the temperature field, surfactant concentration and flow field in the following two limiting conditions: (i) diffusion-dominated surfactant transport considering $Pe_s \ll 1$, and (ii) convection-dominated surfactant transport considering $Pe_s \to \infty$. Analytical expressions for the velocity of a force-free droplet are obtained for both the limits. After studying the effects of different parameters, the following conclusions can be made.

(i) For the case of a neutrally buoyant droplet, low-$Pe_s$ analysis shows that when the imposed temperature field increases in the direction of the Poiseuille flow, a surfactant-laden droplet has both axial (along the direction of the Poiseuille flow) and cross-stream (towards the flow centreline) velocity components. The magnitude of both the components increases with increasing $Ma_T$.

(ii) For a neutrally buoyant droplet, low-$Pe_s$ analysis shows that when the imposed temperature field decreases in the direction of th Poiseuille flow, a surfactant-laden droplet has both axial (in the direction of the Poiseuille flow or opposite to it) and cross-stream (towards or away from the flow centreline) velocity components. There is a critical value of the thermal Marangoni number $Ma^*_{T,z}$ (and $Ma^*_{T,x}$) for which the axial (and cross-stream) velocity vanishes. In sharp contrast to the case of isothermal flow, in which a surfactant-laden droplet always moves towards the flow centreline, a surfactant-laden droplet moves away from the flow centreline for $Ma_T > Ma^*_{T,x}$ in a non-isothermal flow.

(iii) For a neutrally buoyant droplet, high-$Pe_s$ analysis shows that the axial velocity of the droplet is independent of thermal effects. The axial velocity is the same as the velocity of a spherical solid particle. However, the cross-stream motion is strongly dominated by the thermal conductivity ratio ($\delta$) and $Ma_T$. When the imposed temperature field increases in the direction of the Poiseuille flow, the magnitude of the cross-stream velocity (towards the flow centreline) increases with $Ma_T$.

(iv) For a neutrally buoyant droplet, high-$Pe_s$ analysis also shows that when the imposed temperature field decreases in the direction of the Poiseuille flow, a surfactant-laden droplet either moves towards the flow centreline (for $Ma_T < Ma^*_{T,x}$) or moves away from the flow centreline (for $Ma_T > Ma^*_{T,x}$).

(v) Gravity, in the direction of imposed Poiseuille flow, significantly affects the magnitude and direction of the cross-stream migration velocity. For a buoyant droplet having a larger density than the suspending medium, the cross-stream migration characteristics are very similar to those of a neutrally buoyant droplet. Interestingly, when the droplet is less dense than the suspending medium, the droplet can move away from the flow centreline even when the temperature field is increasing in the direction of the Poiseuille flow. For the case of a buoyant droplet, the direction of lateral migration of the droplet can be predicted in a similar manner with respect to the value of $Ma^*_{T,x}$ for both the low- and high-$Pe_s$ limits.

**Acknowledgements**

The authors acknowledge funding from SRIC, Indian Institute of Technology Kharagpur under the Project 'Centre of Excellence for Training and Research in Microfluidics'.

## Appendix A. Velocity and pressure fields in the low $Pe_s$ limit

The leading-order velocity and pressure fields are obtained as

$$\left.\begin{gathered}\boldsymbol{u}_i^{(0)} = \begin{bmatrix} \boldsymbol{\nabla}\times(\boldsymbol{r}\chi_1^{(0)}) + \boldsymbol{\nabla}(\Phi_1^{(0)}+\Phi_2^{(0)}+\Phi_3^{(0)}) \\ +\dfrac{r^2}{\lambda}\boldsymbol{\nabla}\left(\dfrac{1}{5}p_1^{(0)}+\dfrac{5}{42}p_2^{(0)}+\dfrac{1}{12}p_3^{(0)}\right) - \dfrac{\boldsymbol{r}}{\lambda}\left(\dfrac{1}{10}p_1^{(0)}+\dfrac{2}{21}p_2^{(0)}+\dfrac{1}{12}p_3^{(0)}\right) \end{bmatrix}, \\ p_i^{(0)} = p_1^{(0)}+p_2^{(0)}+p_3^{(0)}, \\ \boldsymbol{u}_e^{(0)} = (\boldsymbol{V}_\infty - \boldsymbol{U}^{(0)}) + \begin{bmatrix} \boldsymbol{\nabla}(\Phi_{-2}^{(0)}+\Phi_{-3}^{(0)}+\Phi_{-4}^{(0)}) \\ -r^2\boldsymbol{\nabla}\left(-\dfrac{1}{2}p_{-2}^{(0)}+\dfrac{1}{30}p_{-4}^{(0)}\right) + \boldsymbol{r}\left(2p_{-2}^{(0)}+\dfrac{1}{2}p_{-3}^{(0)}+\dfrac{4}{15}p_{-4}^{(0)}\right) \end{bmatrix}, \\ p_e^{(0)} = p_\infty + (p_{-2}^{(0)}+p_{-3}^{(0)}+p_{-4}^{(0)}).\end{gathered}\right\} \tag{A 1}$$

The growing spherical solid harmonics present in (A 1) are obtained as

$$\left.\begin{gathered}p_1^{(0)} = \lambda r\{A_{1,0}^{(0)}P_{1,0}(\cos\theta) + A_{1,1}^{(0)}\cos\varphi P_{1,1}(\cos\theta) + \hat{A}_{1,1}^{(0)}\sin\varphi P_{1,1}(\cos\theta)\}, \\ p_2^{(0)} = \lambda r^2 A_{2,1}^{(0)}\cos\varphi P_{2,1}(\cos\theta), \quad p_3^{(0)} = \lambda r^3 A_{3,0}^{(0)}P_{3,0}(\cos\theta), \\ \Phi_1^{(0)} = r\{B_{1,0}^{(0)}P_{1,0}(\cos\theta) + B_{1,1}^{(0)}\cos\varphi P_{1,1}(\cos\theta) + \hat{B}_{1,1}^{(0)}\sin\varphi P_{1,1}(\cos\theta)\}, \\ \Phi_2^{(0)} = r^2 B_{2,1}^{(0)}\cos\varphi P_{2,1}(\cos\theta), \quad \Phi_3^{(0)} = r^3 B_{3,0}^{(0)}P_{3,0}(\cos\theta), \\ \chi_1^{(0)} = r\hat{C}_{1,1}^{(0)}\sin\varphi P_{1,1}(\cos\theta),\end{gathered}\right\} \tag{A 2}$$

where the unknown coefficients are obtained as

$$\left.\begin{gathered} A_{1,0}^{(0)}=-\frac{5(2Ma_T T_{1,0}^{(0)}-15\alpha_{1,0}^{(0)}-3\beta_{1,0}^{(0)})}{3\lambda+3}, \quad B_{1,0}^{(0)}=\frac{2Ma_T T_{1,0}^{(0)}-15\alpha_{1,0}^{(0)}-3\beta_{1,0}^{(0)}}{2(3\lambda+3)}, \\ A_{2,1}^{(0)}=\frac{105\beta_{2,1}^{(0)}}{2(5\lambda+5)}, \quad B_{2,1}^{(0)}=-\frac{15\beta_{2,1}^{(0)}}{4(5\lambda+5)}, \quad A_{3,0}^{(0)}=\frac{15\beta_{3,0}^{(0)}}{7(\lambda+1)}, \quad B_{3,0}^{(0)}=-\frac{5\beta_{3,0}^{(0)}}{6(\lambda+1)}, \\ A_{1,1}^{(0)}=\frac{5\beta_{1,1}^{(0)}}{(\lambda+1)}, \quad B_{1,1}^{(0)}=-\frac{\beta_{1,1}^{(0)}}{2(\lambda+1)}, \quad \hat{A}_{1,1}^{(0)}=\frac{5}{(\lambda+1)}\hat{\beta}_{1,1}^{(0)}, \\ \hat{B}_{1,1}^{(0)}=-\frac{\hat{\beta}_{1,1}^{(0)}}{2(\lambda+1)}, \quad \hat{C}_{1,1}^{(0)}=\frac{1}{2}\hat{\gamma}_{1,1}^{(0)}, \end{gathered}\right\} \tag{A 3}$$

with

$$\left.\begin{gathered} T_{1,0}^{(0)}=\frac{3\zeta}{(\delta+2)}, \quad \alpha_{1,0}^{(0)}=-\frac{2}{5R^2}, \quad \beta_{1,0}^{(0)}=1-\left(\frac{e}{R}\right)^2-U_z^{(0)}, \\ \beta_{1,1}^{(0)}=-U_x^{(0)}, \quad \hat{\beta}_{1,1}^{(0)}=-U_y^{(0)}, \quad \beta_{2,1}^{(0)}=-\frac{2}{3}\frac{e}{R^2}, \\ \beta_{3,0}^{(0)}=\frac{2}{5R^2}, \quad \hat{\gamma}_{1,1}^{(0)}=\frac{2e}{R^2}. \end{gathered}\right\} \tag{A 4}$$

The decaying spherical solid harmonics present in (A 1) are obtained as

$$\left.\begin{gathered} p_{-2}^{(0)}=r^{-2}\{A_{-2,0}^{(0)}P_{1,0}(\cos\theta)+A_{-2,1}^{(0)}\cos\varphi P_{1,1}(\cos\theta)+\hat{A}_{-2,1}^{(0)}\sin\varphi P_{1,1}(\cos\theta)\}, \\ p_{-3}^{(0)}=r^{-3}A_{-3,1}^{(0)}\cos\varphi P_{2,1}(\cos\theta), \quad p_{-4}^{(0)}=r^{-4}A_{-4,0}^{(0)}P_{3,0}(\cos\theta), \\ \Phi_{-2}^{(0)}=r^{-2}\{B_{-2,0}^{(0)}P_{1,0}(\cos\theta)+B_{-2,1}^{(0)}\cos\varphi P_{1,1}(\cos\theta)+\hat{B}_{-2,1}^{(0)}\sin\varphi P_{1,1}(\cos\theta)\}, \\ \Phi_{-3}^{(0)}=r^{-3}B_{-3,1}^{(0)}\cos\varphi P_{2,1}(\cos\theta), \quad \Phi_{-4}^{(0)}=r^{-4}B_{-4,0}^{(0)}P_{3,0}(\cos\theta), \end{gathered}\right\} \tag{A 5}$$

where the unknown coefficients are obtained as

$$\left.\begin{gathered} A_{-2,0}^{(0)}=-\frac{2Ma_T T_{1,0}^{(0)}+15\lambda\alpha_{1,0}^{(0)}+9\lambda\beta_{1,0}^{(0)}+6\beta_{1,0}^{(0)}}{6(\lambda+1)}, \quad A_{-2,1}^{(0)}=-\frac{(2+3\lambda)}{2(1+\lambda)}\beta_{1,1}^{(0)}, \\ \hat{A}_{-2,1}^{(0)}=-\frac{(2+3\lambda)}{2(1+\lambda)}\hat{\beta}_{1,1}^{(0)}, \quad B_{-2,0}^{(0)}=-\frac{2Ma_T T_{1,0}^{(0)}+9\lambda\alpha_{1,0}^{(0)}-6\alpha_{1,0}^{(0)}+3\lambda\beta_{1,0}^{(0)}}{12(\lambda+1)}, \\ \hat{B}_{-2,1}^{(0)}=-\frac{\lambda}{4(\lambda+1)}\hat{\beta}_{1,1}^{(0)}, \quad B_{-2,1}^{(0)}=-\frac{\lambda}{4(\lambda+1)}\beta_{1,1}^{(0)}, \\ A_{-3,1}^{(0)}=-\frac{5\lambda\beta_{2,1}^{(0)}+2\beta_{2,1}^{(0)}}{(\lambda+1)}, \quad B_{-3,1}^{(0)}=\frac{-3\lambda\beta_{2,1}^{(0)}}{6(\lambda+1)}, \\ A_{-4,0}^{(0)}=-\frac{35\lambda\beta_{3,0}^{(0)}+10\beta_{3,0}^{(0)}}{4(\lambda+1)}, \quad B_{-4,0}^{(0)}=\frac{-5\lambda\beta_{3,0}^{(0)}}{8(\lambda+1)}. \end{gathered}\right\} \tag{A 6}$$

The far-field pressure field is of the form

$$p_\infty=10r\alpha_{1,0}^{(0)}P_{1,0}(\cos\theta)+7r^2\alpha_{2,1}^{(0)}\cos\varphi P_{2,1}(\cos\theta)+6r^3\alpha_{3,0}^{(0)}P_{3,0}(\cos\theta). \tag{A 7}$$

The $O(Pe_s)$ velocity and pressure fields are obtained as

$$\left.\begin{aligned}
\boldsymbol{u}_i^{(Pe_s)} &= \begin{bmatrix} \boldsymbol{\nabla}(\Phi_1^{(Pe_s)} + \Phi_2^{(Pe_s)} + \Phi_3^{(Pe_s)}) \\ +\dfrac{r^2}{\lambda}\boldsymbol{\nabla}\left(\dfrac{p_1^{(Pe_s)}}{5} + \dfrac{5p_2^{(Pe_s)}}{42} + \dfrac{p_3^{(Pe_s)}}{12}\right) - \dfrac{\boldsymbol{r}}{\lambda}\left(\dfrac{p_1^{(Pe_s)}}{10} + \dfrac{2p_2^{(Pe_s)}}{21} + \dfrac{p_3^{(Pe_s)}}{12}\right) \end{bmatrix}, \\
p_i^{(Pe_s)} &= p_1^{(Pe_s)} + p_2^{(Pe_s)} + p_3^{(Pe_s)}, \\
\boldsymbol{u}_e^{(Pe_s)} &= -\boldsymbol{U}^{(Pe_s)} + \sum_{n=1}^{\infty} \begin{bmatrix} \boldsymbol{\nabla}(\Phi_{-2}^{(Pe_s)} + \Phi_{-3}^{(Pe_s)} + \Phi_{-4}^{(Pe_s)}) \\ -r^2\boldsymbol{\nabla}\left(-\dfrac{p_{-2}^{(Pe_s)}}{2} + \dfrac{p_{-4}^{(Pe_s)}}{30}\right) + \boldsymbol{r}\left(2p_{-2}^{(Pe_s)} + \dfrac{p_{-3}^{(Pe_s)}}{2} + \dfrac{4p_{-4}^{(Pe_s)}}{15}\right) \end{bmatrix}, \\
p_e^{(Pe_s)} &= p_{-2}^{(Pe_s)} + p_{-3}^{(Pe_s)} + p_{-4}^{(Pe_s)}.
\end{aligned}\right\} \tag{A 8}$$

The growing spherical solid harmonics present in (A 8) are obtained as

$$\left.\begin{aligned}
p_1^{(Pe_s)} &= \lambda r\{A_{1,0}^{(Pe_s)}P_{1,0}(\cos\theta) + A_{1,1}^{(Pe_s)}\cos\varphi P_{1,1}(\cos\theta) + \hat{A}_{1,1}^{(Pe_s)}\sin\varphi P_{1,1}(\cos\theta)\}, \\
p_2^{(Pe_s)} &= \lambda r^2 A_{2,1}^{(Pe_s)}\cos\varphi P_{2,1}(\cos\theta), \quad p_3^{(Pe_s)} = \lambda r^3 A_{3,0}^{(Pe_s)}P_{3,0}(\cos\theta), \\
\Phi_1^{(Pe_s)} &= r\{B_{1,0}^{(Pe_s)}P_{1,0}(\cos\theta) + B_{1,1}^{(Pe_s)}\cos\varphi P_{1,1}(\cos\theta) + \hat{B}_{1,1}^{(Pe_s)}\sin\varphi P_{1,1}(\cos\theta)\}, \\
\Phi_2^{(Pe_s)} &= r^2 B_{2,1}^{(Pe_s)}\cos\varphi P_{2,1}(\cos\theta), \quad \Phi_3^{(Pe_s)} = r^3 B_{3,0}^{(Pe_s)}P_{3,0}(\cos\theta),
\end{aligned}\right\} \tag{A 9}$$

where the unknown coefficients are obtained as

$$\left.\begin{aligned}
A_{1,0}^{(Pe_s)} &= -\frac{5\{2Ma_\Gamma\Gamma_{1,0}^{(Pe_s)} - 3\beta_{1,0}^{(Pe_s)}\}}{3(\lambda+1)}, \quad B_{1,0}^{(Pe_s)} = \frac{2Ma_\Gamma\Gamma_{1,0}^{(Pe_s)} - 3\beta_{1,0}^{(Pe_s)}}{2(3\lambda+3)}, \\
A_{1,1}^{(Pe_s)} &= \frac{5\beta_{1,1}^{(Pe_s)}}{(\lambda+1)}, \quad B_{1,1}^{(Pe_s)} = -\frac{\beta_{1,1}^{(Pe_s)}}{2\,(\lambda+1)}, \quad \hat{A}_{1,1}^{(Pe_s)} = \frac{5}{(\lambda+1)}\hat{\beta}_{1,1}^{(Pe_s)}, \\
\hat{B}_{1,1}^{(Pe_s)} &= -\frac{\hat{\beta}_{1,1}^{(Pe_s)}}{2(\lambda+1)}, \quad A_{2,1}^{(Pe_s)} = -\frac{21Ma_\Gamma\Gamma_{2,1}^{(Pe_s)}}{5(\lambda+1)}, \quad B_{2,1}^{(Pe_s)} = \frac{3Ma_\Gamma\Gamma_{2,1}^{(Pe_s)}}{10(\lambda+1)}, \\
A_{3,0}^{(Pe_s)} &= -\frac{36Ma_\Gamma\Gamma_{3,0}^{(Pe_s)}}{7(\lambda+1)}, \quad B_{3,0}^{(Pe_s)} = \frac{2Ma_\Gamma\Gamma_{3,0}^{(Pe_s)}}{7(\lambda+1)},
\end{aligned}\right\} \tag{A 10}$$

with $\beta_{1,0}^{(Pe_s)} = -U_z^{(Pe_s)}$, $\beta_{1,1}^{(Pe_s)} = -U_x^{(Pe_s)}$ and $\hat{\beta}_{1,1}^{(Pe_s)} = -U_y^{(Pe_s)}$.

The decaying spherical solid harmonics present in (A 8) are obtained as

$$\left.\begin{aligned}
p_{-2}^{(Pe_s)} &= r^{-2}\{A_{-2,0}^{(Pe_s)}P_{1,0}(\cos\theta) + A_{-2,1}^{(Pe_s)}\cos\varphi P_{1,1}(\cos\theta) + \hat{A}_{-2,1}^{(Pe_s)}\sin\varphi P_{1,1}(\cos\theta)\}, \\
p_{-3}^{(Pe_s)} &= r^{-3}A_{-3,1}^{(Pe_s)}\cos\varphi P_{2,1}(\cos\theta), \quad p_{-4}^{(Pe_s)} = r^{-4}A_{-4,0}^{(Pe_s)}P_{3,0}(\cos\theta), \\
\Phi_{-2}^{(Pe_s)} &= r^{-2}\{B_{-2,0}^{(Pe_s)}P_{1,0}(\cos\theta) + B_{-2,1}^{(Pe_s)}\cos\varphi P_{1,1}(\cos\theta) + \hat{B}_{-2,1}^{(Pe_s)}\sin\varphi P_{1,1}(\cos\theta)\}, \\
\Phi_{-3}^{(0)} &= r^{-3}B_{-3,1}^{(Pe_s)}\cos\varphi P_{2,1}(\cos\theta), \quad \Phi_{-4}^{(Pe_s)} = r^{-4}B_{-4,0}^{(Pe_s)}P_{3,0}(\cos\theta),
\end{aligned}\right\} \tag{A 11}$$

where the unknown coefficients are obtained as

$$\left.\begin{gathered}
A_{-2,0}^{(Pe_s)}=-\frac{9\lambda\beta_{1,0}^{(Pe_s)}+2Ma_\Gamma\Gamma_{1,0}^{(Pe_s)}+6\beta_{1,0}^{(Pe_s)}}{6(\lambda+1)},\quad A_{-2,1}^{(Pe_s)}=-\frac{(2+3\lambda)}{2(1+\lambda)}\beta_{1,1}^{(Pe_s)},\\
\hat{A}_{-2,1}^{(0)}=-\frac{(2+3\lambda)}{2(1+\lambda)}\hat{\beta}_{1,1}^{(Pe_s)},\quad B_{-2,0}^{(Pe_s)}=-\frac{2Ma_\Gamma\Gamma_{1,0}^{(Pe_s)}+3\lambda\beta_{1,0}^{(Pe_s)}}{12(\lambda+1)},\\
\hat{B}_{-2,1}^{(Pe_s)}=-\frac{\lambda}{4(\lambda+1)}\hat{\beta}_{1,1}^{(Pe_s)},\quad B_{-2,1}^{(Pe_s)}=-\frac{\lambda}{4(\lambda+1)}\beta_{1,1}^{(Pe_s)},\\
A_{-3,1}^{(Pe_s)}=-\frac{6Ma_\Gamma\Gamma_{2,1}^{(Pe_s)}}{5(\lambda+1)},\quad B_{-3,1}^{(Pe_s)}=-\frac{Ma_\Gamma\Gamma_{2,1}^{(Pe_s)}}{5(\lambda+1)},\\
A_{-4,0}^{(Pe_s)}=-\frac{15Ma_\Gamma\Gamma_{3,0}^{(Pe_s)}}{7(\lambda+1)},\quad B_{-4,0}^{(Pe_s)}=-\frac{3Ma_\Gamma\Gamma_{3,0}^{(Pe_s)}}{14(\lambda+1)}.
\end{gathered}\right\}\tag{A 12}$$

The $O(Pe_s^2)$ velocity and pressure fields are obtained as

$$\left.\begin{gathered}
\boldsymbol{u}_i^{(Pe_s^2)}=\begin{bmatrix}\nabla(\Phi_1^{(Pe_s^2)}+\Phi_2^{(Pe_s^2)}+\Phi_3^{(Pe_s^2)})+\dfrac{r^2}{\lambda}\nabla\left(\dfrac{1}{5}p_1^{(Pe_s^2)}+\dfrac{5}{42}p_2^{(Pe_s^2)}+\dfrac{1}{12}p_3^{(Pe_s^2)}\right)\\ -\dfrac{\boldsymbol{r}}{\lambda}\left(\dfrac{1}{10}p_1^{(Pe_s^2)}+\dfrac{2}{21}p_2^{(Pe_s^2)}+\dfrac{1}{12}p_3^{(Pe_s^2)}\right)\end{bmatrix},\\
p_i^{(Pe_s^2)}=p_1^{(Pe_s^2)}+p_2^{(Pe_s^2)}+p_3^{(Pe_s^2)},\\
\boldsymbol{u}_e^{(Pe_s^2)}=-\boldsymbol{U}^{(Pe_s^2)}+\sum_{n=1}^{\infty}\begin{bmatrix}\nabla(\Phi_{-2}^{(Pe_s^2)}+\Phi_{-3}^{(Pe_s^2)}+\Phi_{-4}^{(Pe_s^2)})-r^2\nabla\left(-\dfrac{1}{2}p_{-2}^{(Pe_s^2)}+\dfrac{1}{30}p_{-4}^{(Pe_s^2)}\right)\\ +\boldsymbol{r}\left(2p_{-2}^{(Pe_s^2)}+\dfrac{1}{2}p_{-3}^{(Pe_s^2)}+\dfrac{4}{15}p_{-4}^{(Pe_s^2)}\right)\end{bmatrix},\\
p_e^{(Pe_s^2)}=p_{-2}^{(Pe_s^2)}+p_{-3}^{(Pe_s^2)}+p_{-4}^{(Pe_s^2)}.
\end{gathered}\right\}\tag{A 13}$$

The growing spherical solid harmonics present in (A 13) are obtained as

$$\left.\begin{gathered}
p_1^{(Pe_s^2)}=\lambda r\{A_{1,0}^{(Pe_s^2)}P_{1,0}(\cos\theta)+A_{1,1}^{(Pe_s^2)}\cos\varphi P_{1,1}(\cos\theta)+\hat{A}_{1,1}^{(Pe_s^2)}\sin\varphi P_{1,1}(\cos\theta)\},\\
p_2^{(Pe_s^2)}=\lambda r^2A_{2,1}^{(Pe_s^2)}\cos\varphi P_{2,1}(\cos\theta),\\
p_3^{(Pe_s^2)}=\lambda r^3\{A_{3,0}^{(Pe_s^2)}P_{3,0}(\cos\theta)+A_{3,1}^{(Pe_s^2)}\cos\varphi P_{3,1}(\cos\theta)\},\\
\Phi_1^{(Pe_s^2)}=r\{B_{1,0}^{(Pe_s^2)}P_{1,0}(\cos\theta)+B_{1,1}^{(Pe_s^2)}\cos\varphi P_{1,1}(\cos\theta)+\hat{B}_{1,1}^{(Pe_s^2)}\sin\varphi P_{1,1}(\cos\theta)\},\\
\Phi_2^{(Pe_s^2)}=r^2B_{2,1}^{(Pe_s^2)}\cos\varphi P_{2,1}(\cos\theta),\\
\Phi_3^{(Pe_s^2)}=r^3\{B_{3,0}^{(Pe_s)}P_{3,0}(\cos\theta)+B_{3,1}^{(Pe_s^2)}\cos\varphi P_{3,1}(\cos\theta)\},
\end{gathered}\right\}\tag{A 14}$$

where the unknown coefficients are obtained as

$$\left.\begin{gathered}
A_{1,0}^{(Pe_s^2)}=-\frac{5(2Ma_\Gamma\Gamma_{1,0}^{(Pe_s^2)}-3\beta_{1,0}^{(Pe_s^2)})}{3(\lambda+1)},\quad B_{1,0}^{(Pe_s^2)}=\frac{2Ma_\Gamma\Gamma_{1,0}^{(Pe_s^2)}-3\beta_{1,0}^{(Pe_s^2)}}{6(\lambda+1)},\\
A_{1,1}^{(Pe_s^2)}=-\frac{5(2Ma_\Gamma\Gamma_{1,1}^{(Pe_s^2)}-3\beta_{1,1}^{(Pe_s^2)})}{3(\lambda+1)},\quad B_{1,1}^{(Pe_s)}=\frac{2Ma_\Gamma\Gamma_{1,1}^{(Pe_s^2)}-3\beta_{1,1}^{(Pe_s^2)}}{6(\lambda+1)},
\end{gathered}\right\}\tag{A 15}$$

$$\left.\begin{gathered}\hat{A}_{1,1}^{(Pe_s)}=\frac{5}{(\lambda+1)}\hat{\beta}_{1,1}^{(Pe_s)},\quad \hat{B}_{1,1}^{(Pe_s)}=-\frac{\hat{\beta}_{1,1}^{(Pe_s)}}{2(\lambda+1)},\quad A_{2,1}^{(Pe_s^2)}=-\frac{21Ma_\Gamma\Gamma_{2,1}^{(Pe_s^2)}}{5(\lambda+1)},\\ B_{2,1}^{(Pe_s^2)}=\frac{3Ma_\Gamma\Gamma_{2,1}^{(Pe_s^2)}}{10(\lambda+1)},\quad A_{3,0}^{(Pe_s^2)}=-\frac{36Ma_\Gamma\Gamma_{3,0}^{(Pe_s^2)}}{7(\lambda+1)},\quad B_{3,0}^{(Pe_s^2)}=\frac{2Ma_\Gamma\Gamma_{3,0}^{(Pe_s^2)}}{7(\lambda+1)},\\ A_{3,1}^{(Pe_s^2)}=-\frac{36Ma_\Gamma\Gamma_{3,1}^{(Pe_s^2)}}{7(\lambda+1)},\quad B_{3,1}^{(Pe_s^2)}=\frac{2Ma_\Gamma\Gamma_{3,1}^{(Pe_s^2)}}{7(\lambda+1)},\end{gathered}\right\}\tag{A 16}$$

with $\beta_{1,0}^{(Pe_s^2)}=-U_z^{(Pe_s^2)}$, $\beta_{1,1}^{(Pe_s^2)}=-U_x^{(Pe_s^2)}$ and $\hat{\beta}_{1,1}^{(Pe_s^2)}=-U_y^{(Pe_s^2)}$. The different constants present in the expression of surfactant concentration ($\Gamma_{n,m}^{(Pe_s^2)}$) for $O(Pe_s^2)$ are given in appendix B. The decaying spherical solid harmonics present in (A 13) are obtained as

$$\left.\begin{gathered}p_{-2}^{(Pe_s^2)}=r^{-2}\{A_{-2,0}^{(Pe_s^2)}P_{1,0}(\cos\theta)+A_{-2,1}^{(Pe_s^2)}\cos\varphi P_{1,1}(\cos\theta)+\hat{A}_{-2,1}^{(Pe_s^2)}\sin\varphi P_{1,1}(\cos\theta)\},\\ p_{-3}^{(Pe_s^2)}=r^{-3}A_{-3,1}^{(Pe_s^2)}\cos\varphi P_{2,1}(\cos\theta),\\ p_{-4}^{(Pe_s^2)}=r^{-4}\{A_{-4,0}^{(Pe_s^2)}P_{3,0}(\cos\theta)+A_{-4,1}^{(Pe_s^2)}\cos\varphi P_{3,1}(\cos\theta)\},\\ \Phi_{-2}^{(Pe_s^2)}=r^{-2}\{B_{-2,0}^{(Pe_s^2)}P_{1,0}(\cos\theta)+B_{-2,1}^{(Pe_s^2)}\cos\varphi P_{1,1}(\cos\theta)+\hat{B}_{-2,1}^{(Pe_s^2)}\sin\varphi P_{1,1}(\cos\theta)\},\\ \Phi_{-3}^{(0)}=r^{-3}B_{-3,1}^{(Pe_s^2)}\cos\varphi P_{2,1}(\cos\theta),\\ \Phi_{-4}^{(Pe_s^2)}=r^{-4}\{B_{-4,0}^{(Pe_s^2)}P_{3,0}(\cos\theta)+B_{-4,1}^{(Pe_s^2)}\cos\varphi P_{3,1}(\cos\theta)\},\end{gathered}\right\}\tag{A 17}$$

where the unknown coefficients are obtained as

$$\left.\begin{gathered}A_{-2,0}^{(Pe_s^2)}=-\frac{9\lambda\beta_{1,0}^{(Pe_s^2)}+2Ma_\Gamma\Gamma_{1,0}^{(Pe_s^2)}+6\beta_{1,0}^{(Pe_s^2)}}{6(\lambda+1)},\\ A_{-2,1}^{(Pe_s^2)}=-\left\{\frac{Ma_\Gamma\Gamma_{1,1}^{(Pe_s^2)}}{3(\lambda+1)}+\frac{3\lambda+2}{2(\lambda+1)}\beta_{1,1}^{(Pe_s^2)}\right\}\\ \hat{A}_{-2,1}^{(Pe_s^2)}=-\frac{3\lambda+2}{2(\lambda+1)}\hat{\beta}_{1,1}^{(Pe_s^2)},\quad B_{-2,1}^{(Pe_s^2)}=-\left\{\frac{Ma_\Gamma\Gamma_{1,1}^{(Pe_s^2)}}{6(\lambda+1)}+\frac{\lambda}{4(\lambda+1)}\beta_{1,1}^{(Pe_s^2)}\right\},\\ \hat{B}_{-2,1}^{(Pe_s^2)}=-\frac{\lambda}{4(\lambda+1)}\hat{\beta}_{1,1}^{(Pe_s^2)},\quad B_{-2,0}^{(Pe_s^2)}=-\frac{2Ma_\Gamma\Gamma_{1,0}^{(Pe_s^2)}+3\lambda\beta_{1,0}^{(Pe_s^2)}}{12(\lambda+1)},\\ A_{-3,1}^{(Pe_s^2)}=-\frac{6Ma_\Gamma\Gamma_{2,1}^{(Pe_s^2)}}{5(\lambda+1)},\quad B_{-3,1}^{(Pe_s^2)}=-\frac{Ma_\Gamma\Gamma_{2,1}^{(Pe_s^2)}}{5(\lambda+1)},\\ A_{-4,1}^{(Pe_s^2)}=-\frac{15Ma_\Gamma\Gamma_{3,1}^{(Pe_s^2)}}{7(\lambda+1)},\quad B_{-4,1}^{(Pe_s^2)}=-\frac{3Ma_\Gamma\Gamma_{3,1}^{(Pe_s^2)}}{14(\lambda+1)},\\ A_{-4,0}^{(Pe_s^2)}=-\frac{15Ma_\Gamma\Gamma_{3,0}^{(Pe_s^2)}}{7(\lambda+1)},\quad B_{-4,0}^{(Pe_s^2)}=-\frac{3Ma_\Gamma\Gamma_{3,0}^{(Pe_s^2)}}{14(\lambda+1)}.\end{gathered}\right\}\tag{A 18}$$

## Appendix B. Expressions for the constant coefficients present in (3.24) for surfactant concentration of $O(Pe_s^2)$

The coefficients present in the $O(Pe_s^2)$ surface harmonics of surfactant concentration are obtained as

$$\left.\begin{aligned}
\Gamma_{1,0}^{(Pe_s^2)} &= \frac{\xi Bo}{3Ca}\frac{Ma_\Gamma}{(3\lambda+2)^2}+\frac{(2\delta+3Ma_T\zeta R^2+4)Ma_\Gamma}{(9\delta\lambda^2+12\delta\lambda+4\delta+18\lambda^2+8+24\lambda)R^2},\\
\Gamma_{1,1}^{(Pe_s^2)} &= -\frac{\xi Bo}{30Ca}\frac{(5\lambda+3)}{(\lambda+1)(3\lambda+2)}\frac{e}{R^2}\\
&\quad -\frac{\begin{pmatrix}70\delta\lambda^2+109\delta\lambda+40\delta+140\lambda^2+218\lambda+80\\ +105Ma_T\zeta R^2\lambda^2+168Ma_T\zeta R^2\lambda+63Ma_T\zeta R^2\end{pmatrix}e}{70(7\delta\lambda+8\delta\lambda^2+3\delta\lambda^3+2\delta+6\lambda^3+16\lambda^2+4+14\lambda)R^4},\\
\Gamma_{2,0}^{(Pe_s^2)} &= \left[\begin{aligned}&\frac{\xi Bo}{Ca}\left\{\frac{\xi Bo}{27Ca(3\lambda+2)^2}+\frac{(47\lambda+50)}{126R^2(\lambda+1)(3\lambda+2)^2}+\frac{2}{3}\frac{\zeta Ma_T}{(3\lambda+2)^2(\delta+2)}\right\}\\ &+\frac{\begin{Bmatrix}1134(\lambda+1)^2Ma_T^2\zeta^2R^4+27(47\lambda+50)(\lambda+1)(\delta+2)Ma_T\zeta R^2\\ +(\delta+2)^2\,(\,567e^2\lambda^3+750\lambda+1404e^2\lambda^2+288e^2+400+351\lambda^2\\ +1116e^2\lambda\,)\end{Bmatrix}}{378R^4(\lambda+1)^2(3\lambda+2)^2(\delta+2)^2}\end{aligned}\right],\\
\Gamma_{2,1}^{(Pe_s^2)} &= \frac{1}{15}\frac{Ma_\Gamma e}{(\lambda^2+2\lambda+1)R^2},\quad \Gamma_{2,2}^{(Pe_s^2)}=-\frac{1}{252}\frac{(7\lambda+4)e^2}{(\lambda^2+2\lambda+1)R^4},\\
\Gamma_{3,0}^{(Pe_s^2)} &= -\frac{1}{42}\frac{Ma_\Gamma}{R^2(\lambda^2+2\lambda+1)},\\
\Gamma_{3,1}^{(Pe_s^2)} &= \frac{2\xi Bo}{45Ca}\frac{e}{R^2(3\lambda^2+5\lambda+2)}\\
&\quad +\frac{[432(\lambda+1)Ma_T\zeta R^2+(45\lambda^2+351\lambda+310)(\delta+2)]e}{1080(3\lambda+2)(\lambda+1)^2(\delta+2)R^4}.
\end{aligned}\right\}\tag{B 1}$$

## Appendix C. Velocity and pressure fields in the high-$Pe_s$ limit

The leading-order velocity and pressure fields are obtained as

$$\left.\begin{aligned}
\boldsymbol{u}_i^{(0)} &= \boldsymbol{\nabla}\times(\boldsymbol{r}\chi_1^{(0)}),\\
p_i^{(0)} &= 0,\\
\boldsymbol{u}_e^{(0)} &= (\boldsymbol{V}_\infty-\boldsymbol{U}^{(0)})+\sum_{n=1}^{\infty}\left[\begin{aligned}&\boldsymbol{\nabla}(\Phi_{-2}^{(0)}+\Phi_{-3}^{(0)}+\Phi_{-4}^{(0)})\\ &-r^2\boldsymbol{\nabla}\left(-\frac{p_{-2}^{(0)}}{2}+\frac{p_{-4}^{(0)}}{30}\right)+\boldsymbol{r}\left(2p_{-2}^{(0)}+\frac{p_{-3}^{(0)}}{2}+\frac{4p_{-4}^{(0)}}{15}\right)\end{aligned}\right],\\
p_e^{(0)} &= p_\infty+(p_{-2}^{(0)}+p_{-3}^{(0)}+p_{-4}^{(0)}).
\end{aligned}\right\}\tag{C 1}$$

The growing spherical solid harmonics present in (C 1) are obtained as

$$\chi_1^{(0)}=\tfrac{1}{2}\hat{\gamma}_{1,1}^{(0)}r\sin\varphi P_{1,1}(\cos\theta).\tag{C 2}$$

The decaying spherical solid harmonics present in (C 1) are obtained as

$$\left.\begin{gathered} p_{-2}^{(0)} = r^{-2}\{A_{-2,0}^{(0)} P_{1,0}(\cos\theta) + A_{-2,1}^{(0)} \cos\varphi P_{1,1}(\cos\theta) + \hat{A}_{-2,1}^{(0)} \sin\varphi P_{1,1}(\cos\theta)\}, \\ p_{-3}^{(0)} = r^{-3} A_{-3,1}^{(0)} \cos\varphi P_{2,1}(\cos\theta), \quad p_{-4}^{(0)} = r^{-4} A_{-4,0}^{(0)} P_{3,0}(\cos\theta), \\ \Phi_{-2}^{(0)} = r^{-2}\{B_{-2,0}^{(0)} P_{1,0}(\cos\theta) + B_{-2,1}^{(0)} \cos\varphi P_{1,1}(\cos\theta) + \hat{B}_{-2,1}^{(0)} \sin\varphi P_{1,1}(\cos\theta)\}, \\ \Phi_{-3}^{(0)} = r^{-3} B_{-3,1}^{(0)} \cos\varphi P_{2,1}(\cos\theta), \quad \Phi_{-4}^{(0)} = r^{-4} B_{-4,0}^{(0)} P_{3,0}(\cos\theta), \end{gathered}\right\} \tag{C 3}$$

where the unknown coefficients are obtained as

$$\left.\begin{gathered} A_{-2,0}^{(0)} = -\tfrac{5}{2}\alpha_{1,0}^{(0)} - \tfrac{3}{2}\beta_{1,0}^{(0)}, \quad A_{-2,1}^{(0)} = -\tfrac{3}{2}\beta_{1,1}^{(0)}, \quad \hat{A}_{-2,1}^{(0)} = -\tfrac{3}{2}\hat{\beta}_{1,1}^{(0)}, \\ B_{-2,0}^{(0)} = -\tfrac{3}{4}\alpha_{1,0}^{(0)} - \tfrac{1}{4}\beta_{1,0}^{(0)}, \quad B_{-2,1}^{(0)} = -\tfrac{1}{4}\beta_{1,1}^{(0)}, \quad A_{-3,1}^{(0)} = -5\beta_{2,1}^{(0)}, \\ B_{-3,1}^{(0)} = -\tfrac{1}{2}\beta_{2,1}^{(0)}, \quad A_{-4,0}^{(0)} = -\tfrac{35}{4}\beta_{3,0}^{(0)}, \quad B_{-4,0}^{(0)} = -\tfrac{5}{8}\beta_{3,0}^{(0)}. \end{gathered}\right\} \tag{C 4}$$

## REFERENCES


AHN, K., KERBAGE, C., HUNT, T. P., WESTERVELT, R. M., LINK, D. R. & WEITZ, D. A. 2006 Dielectrophoretic manipulation of drops for high-speed microfluidic sorting devices. *Appl. Phys. Lett.* **88** (2), 24104.

AMINI, H., LEE, W. & DI CARLO, D. 2014 Inertial microfluidic physics. *Lab on a Chip* **14** (15), 2739–2761.

BALASUBRAMANIAM, R. & SUBRAMANIAN, R. S. 2004 Thermocapillary convection due to a stationary bubble. *Phys. Fluids* **16** (8), 3131–3137.

BANDOPADHYAY, A., MANDAL, S., KISHORE, N. K. & CHAKRABORTY, S. 2016 Uniform electric-field-induced lateral migration of a sedimenting drop. *J. Fluid Mech.* **792**, 553–589.

BARET, J.-C. 2012 Surfactants in droplet-based microfluidics. *Lab on a Chip* **12** (3), 422–433.

BAROUD, C. N., DELVILLE, J. P., GALLAIRE, F. & WUNENBURGER, R. 2007 Thermocapillary valve for droplet production and sorting. *Phys. Rev.* E **75** (4), 46302.

BAROUD, C. N., GALLAIRE, F. & DANGLA, R. 2010 Dynamics of microfluidic droplets. *Lab on a Chip* **10** (16), 2032–2045.

BARTON, K. D. & SHANKAR SUBRAMANIAN, R. 1990 Thermocapillary migration of a liquid drop normal to a plane surface. *J. Colloid Interface Sci.* **137** (1), 170–182.

BARTON, K. D. & SUBRAMANIAN, R. S. 1991 Migration of liquid drops in a vertical temperature gradient-interaction effects near a horizontal surface. *J. Colloid Interface Sci.* **141** (1), 146–156.

BONNER, W. A., HULETT, H. R., SWEET, R. G. & HERZENBERG, L. A. 1972 Fluorescence activated cell sorting. *Rev. Sci. Instrum.* **43** (3), 404–409.

DI CARLO, D., IRIMIA, D., TOMPKINS, R. G. & TONER, M. 2007 Continuous inertial focusing, ordering, and separation of particles in microchannels. *Proc. Natl Acad. Sci. USA* **104** (48), 18892–18897.

CARPENTER, B. & HOMSY, G. M. 1985 The effect of surface contamination on thermocapillary flow in a two-dimensional slot. Part 2. Partially contaminated interfaces. *J. Fluid Mech.* **155**, 429–439.

CASADEVALL I SOLVAS, X. & DEMELLO, A. 2011 Droplet microfluidics: recent developments and future applications. *Chem. Commun. (Camb).* **47** (7), 1936–1942.

CHAN, P. C.-H. & LEAL, L. G. 1979 The motion of a deformable drop in a second-order fluid. *J. Fluid Mech.* **92** (1), 131–170.

CHEN, S. H. 1999 Thermocapillary migration of a fluid sphere parallel to an insulated plane. *Langmuir* **15** (25), 8618–8626.

CHEN, S. H. 2003 Thermocapillary coagulations of a fluid sphere and a gas bubble. *Langmuir* **19** (11), 4582–4591.

CHEN, X., XUE, C., ZHANG, L., HU, G., JIANG, X. & SUN, J. 2014 Inertial migration of deformable droplets in a microchannel. *Phys. Fluids* **26** (11), 112003.

CHEN, Y. S., LU, Y. L., YANG, Y. M. & MAA, J. R. 1997 Surfactant effects on the motion of a droplet in thermocapillary migration. *Intl J. Multiphase Flow* **23** (2), 325–335.

CHOUDHURI, D. & RAJA SEKHAR, G. P. 2013 Thermocapillary drift on a spherical drop in a viscous fluid. *Phys. Fluids* **25** (4), 043104.

DAS, S., MANDAL, S., SOM, S. K. & CHAKRABORTY, S. 2017 Migration of a surfactant-laden droplet in non-isothermal Poiseuille flow. *Phys. Fluids* **29** (1), 12002.

FÅHRAEUS, R. 1929 The suspension stability of the blood. *Phys. Rev.* **9**, 241–274.

GIDDINGS, J. 1993 Field-flow fractionation: analysis of macromolecular, colloidal, and particulate materials. *Science* **260** (5113), 1456–1465.

GRIGGS, A. J., ZINCHENKO, A. Z. & DAVIS, R. H. 2007 Low-Reynolds-number motion of a deformable drop between two parallel plane walls. *Intl J. Multiphase Flow* **33** (2), 182–206.

HABER, S. & HETSRONI, G. 1971 The dynamics of a deformable drop suspended in an unbounded Stokes flow. *J. Fluid Mech.* **49** (2), 257–277.

HABER, S. & HETSRONI, G. 1972 Hydrodynamics of a drop submerged in an unbounded arbitrary velocity field in the presence of surfactants. *Appl. Sci. Res.* **25** (1), 215–233.

HÄHNEL, M., DELITZSCH, V. & ECKELMANN, H. 1989 The motion of droplets in a vertical temperature gradient. *Phys. Fluids* A **1** (9), 1460–1466.

HAJ-HARIRI, H., NADIM, A. & BORHAN, A. 1990 Effect of inertia on the thermocapillary velocity of a drop. *J. Colloid Interface Sci.* **140** (1), 277–286.

HANNA, J. A. & VLAHOVSKA, P. M. 2010 Surfactant-induced migration of a spherical drop in Stokes flow. *Phys. Fluids* **22** (1), 013102.

HAPPEL, J. & BRENNER, H. 1981 *Low Reynolds Number Hydrodynamics*. Springer.

HATCH, A. C., PATEL, A., BEER, N. R. & LEE, A. P. 2013 Passive droplet sorting using viscoelastic flow focusing. *Lab on a Chip* **13**, 1308–1315.

HETSRONI, G. & HABER, S. 1970 The flow in and around a droplet or bubble submerged in an unbound arbitrary velocity field. *Rheol. Acta* **9** (4), 488–496.

HOMSY, G. & MEIBURG, E. 1984 The effect of surface contamination on thermocapillary flow in a two-dimensional slot. *J. Fluid Mech.* **139**, 443–459.

HUEBNER, A., SHARMA, S., SRISA-ART, M., HOLLFELDER, F., EDEL, J. B. & DEMELLO, A. J. 2008 Microdroplets: a sea of applications? *Lab on a Chip* **8** (8), 1244–1254.

HUR, S. C., HENDERSON-MACLENNAN, N. K., MCCABE, E. R. B. & DI CARLO, D. 2011 Deformability-based cell classification and enrichment using inertial microfluidics. *Lab on a Chip* **11** (5), 912–920.

KARABELAS, A. J. 1977 Vertical distribution of dilute suspensions in turbulent pipe flow. *AIChE J.* **23** (4), 426–434.

KARBALAEI, A., KUMAR, R. & CHO, H. J. 2016 Thermocapillarity in microfluidics: a review. *Micromachines* **7** (1), 1–41.

KARNIS, A., GOLDSMITH, H. L. & MASON, S. G. 1966 The flow of suspensions through tubes. Part V. Inertial effects. *Can. J. Chem. Engng* **44** (4), 181–193.

KAUSHAL, D. & TOMITA, Y. 2002 Solids concentration profiles and pressure drop in pipeline flow of multisized particulate slurries. *Intl J. Multiphase Flow* **28** (10), 1697–1717.

KIM, H. S. & SUBRAMANIAN, R. S. 1989*a* The thermocapillary migration of a droplet with insoluble surfactant. Part II. General case. *J. Colloid Interface Sci.* **130** (1), 112–129.

KIM, H. S. & SUBRAMANIAN, R. S. 1989*b* Thermocapillary migration of a droplet with insoluble surfactant. Part I. Surfactant cap. *J. Colloid Interface Sci.* **127** (2), 417–428.

LEAL, L. G. 1980 Particle motions in a viscous fluid. *Annu. Rev. Fluid Mech.* **12** (1), 435–476.

LEAL, L. G. 2007 *Advanced Transport Phenomena*. Cambridge University Press.

LINK, D. R., GRASLAND-MONGRAIN, E., DURI, A., SARRAZIN, F., CHENG, Z., CRISTOBAL, G., MARQUEZ, M. & WEITZ, D. A. 2006 Electric control of droplets in microfluidic devices. *Angew. Chem. Intl Ed.* **45** (16), 2556–2560.

MANDAL, S., BANDOPADHYAY, A. & CHAKRABORTY, S. 2015 Effect of interfacial slip on the cross-stream migration of a drop in an unbounded Poiseuille flow. *Phys. Rev.* E **92** (2), 23002.

MANDAL, S., BANDOPADHYAY, A. & CHAKRABORTY, S. 2016 Effect of surface charge convection and shape deformation on the dielectrophoretic motion of a liquid drop. *Phys. Rev.* E **93**, 43127.

MEYYAPPAN, M. & SUBRAMANIAN, R. S. 1987 Thermocapillary migration of a gas bubble in an arbitrary direction with respect to a plane surface. *J. Colloid Interface Sci.* **115** (1), 206–219.

MIRALLES, V., HUERRE, A., MALLOGGI, F. & JULLIEN, M. 2013 A review of heating and temperature control in microfluidic systems: techniques and applications. *Diagnostics* **3**, 33–67.

MORTAZAVI, S. & TRYGGVASON, G. 2000 A numerical study of the motion of drops in Poiseuille flow. Part 1. Lateral migration of one drop. *J. Fluid Mech.* **411**, 325–350.

MUKHERJEE, S. & SARKAR, K. 2013 Effects of matrix viscoelasticity on the lateral migration of a deformable drop in a wall-bounded shear. *J. Fluid Mech.* **727**, 318–345.

MUKHERJEE, S. & SARKAR, K. 2014 Lateral migration of a viscoelastic drop in a Newtonian fluid in a shear flow near a wall. *Phys. Fluids* **26** (10), 103102.

NADIM, A., HAJ-HARIRI, H. & BORHAN, A. 1990 Thermocapillary migration of slightly deformed droplets. *Part. Sci. Technol.* **8** (3–4), 191–198.

NALLANI, M. & SUBRAMANIAN, R. S. 1993 Migration of methanol drops in a vertical temperature gradient in a silicone oil. *J. Colloid Interface Sci.* **157** (1), 24–31.

PAK, O. S., FENG, J. & STONE, H. A. 2014 Viscous Marangoni migration of a drop in a Poiseuille flow at low surface Péclet numbers. *J. Fluid Mech.* **753**, 535–552.

PRIES, A., SECOMB, T. & GAEHTGENS, P. 1996 Biophysical aspects of blood flow in the microvasculature. *Cardiovasc. Res.* **32**, 654–667.

ROBERT DE SAINT VINCENT, M., WUNENBURGER, R. & DELVILLE, J. 2008 Laser switching and sorting for high speed digital microfluidics. *Appl. Phys. Lett.* **92**, 154105.

SAJEESH, P. & SEN, A. K. 2014 Particle separation and sorting in microfluidic devices: a review. *Microfluid Nanofluid.* **17** (1), 1–52.

SCHWALBE, J. T., PHELAN, F. R. JR, VLAHOVSKA, P. M. & HUDSON, S. D. 2011 Interfacial effects on droplet dynamics in Poiseuille flow. *Soft Matt.* **7** (17), 7797.

SEEMANN, R., BRINKMANN, M., PFOHL, T. & HERMINGHAUS, S. 2012 Droplet based microfluidics. *Rep. Prog. Phys.* **75** (75), 16601–16641.

SEKHAR, G. P. R., SHARANYA, V. & ROHDE, C. 2016 Effect of surfactant concentration and interfacial slip on the flow past a viscous drop at low surface Péclet number. arXiv:1609.03410.

SHARANYA, V. & RAJA SEKHAR, G. P. 2015 Thermocapillary migration of a spherical drop in an arbitrary transient Stokes flow. *Phys. Fluids* **27** (6), 063104.

SHIELDS, C. W., REYES, C. D. & LÓPEZ, G. P. 2015 Microfluidic cell sorting: a review of the advances in the separation of cells from debulking to rare cell isolation. *Lab on a Chip* **15** (5), 1230–1249.

STAN, C. A., GUGLIELMINI, L., ELLERBEE, A. K., CAVIEZEL, D., STONE, H. A. & WHITESIDES, G. M. 2011 Sheathless hydrodynamic positioning of buoyant drops and bubbles inside microchannels. *Phys. Rev.* E **84** (3), 1–21.

STEBE, K. J., LIN, S. Y. & MALDARELLI, C. 1991 Remobilizing surfactant retarded fluid particle interfaces. Part 1. Stress-free conditions at the interfaces of micellar solutions of surfactants with fast sorption kinetics. *Phys. Fluids* A **3** (1991), 3–20.

STONE, H. A. 1990 A simple derivation of the time-dependent convective-diffusion equation for surfactant transport along a deforming interface. *Phys. Fluids* A **2** (1), 111–112.

STONE, H. A. & LEAL, L. G. 1990 The effects of surfactants on drop deformation and breakup. *J. Fluid Mech.* **220**, 161–186.

STONE, H. A., STROOCK, A. D. & AJDARI, A. 2004 Engineering flows in small devices. *Annu. Rev. Fluid Mech.* **36** (1), 381–411.

TEH, S.-Y., LIN, R., HUNG, L.-H. & LEE, A. P. 2008 Droplet microfluidics. *Lab on a Chip* **8** (2), 198–220.

VLAHOVSKA, P. M., BŁAWZDZIEWICZ, J. & LOEWENBERG, M. 2009 Small-deformation theory for a surfactant-covered drop in linear flows. *J. Fluid Mech.* **624**, 293.

VLAHOVSKA, P. M., LOEWENBERG, M. & BLAWZDZIEWICZ, J. 2005 Deformation of a surfactant-covered drop in a linear flow. *Phys. Fluids* **17** (10), 103103.

WOHL, P. R. & RUBINOW, S. I. 1974 The transverse force on a drop in an unbounded parabolic flow. *J. Fluid Mech.* **62** (1), 185–207.

YANG, J., HUANG, Y., WANG, X.-B., BECKER, F. F. & GASCOYNE, P. R. C. 1999 Cell separation on microfabricated electrodes using dielectrophoretic/gravitational field-flow fractionation. *Anal. Chem.* **71** (5), 911–918.

YARIV, E. & SHUSSER, M. 2006 On the paradox of thermocapillary flow about a stationary bubble. *Phys. Fluids* **18** (7), 072101.

YOUNG, N. O., GOLDSTEIN, J. S. & BLOCK, M. J. 1959 The motion of bubbles in a vertical temperature gradient. *J. Fluid Mech.* **6** (3), 350–356.

ZHANG, L., SUBRAMANIAN, R. S. & BALASUBRAMANIAM, R. 2001 Motion of a drop in a vertical temperature gradient at small Marangoni number: the critical role of inertia. *J. Fluid Mech.* **448**, 197–211.

ZHU, Y. & FANG, Q. 2013 Analytical detection techniques for droplet microfluidics: a review. *Anal. Chim. Acta* **787**, 24–35.